Integral field spectroscopy of the planetary nebula NGC 3242 and the puzzling nature of its low-ionization structures

Konstantinou, L.; Akras, S.; Garcia-Rojas, J.; Bouvis, K.; Gonçalves, D.R.; Monteiro, H.; ... ; Monreal Ibero, A.

A&A, 697, A227 (2025)
https://doi.org/10.1051/0004-6361/202453635

Astronomy & Astrophysics

Integral field spectroscopy of the planetary nebula NGC 3242 and the puzzling nature of its low-ionization structures

L. Konstantinou[1,2,⋆], S. Akras[1], J. Garcia-Rojas[3,4], K. Bouvis[1,2], D. R. Gonçalves[5], H. Monteiro[6,7], P. Boumis[1], M. B. Mari[8], I. Aleman[9], and A. Monreal-Ibero[10]

[1] Institute for Astronomy, Astrophysics, Space Applications and Remote Sensing, National Observatory of Athens, 15236 Penteli, Greece
[2] Department of Physics, University of Patras, Patras, 26504 Rio, Greece
[3] Instituto de Astrofísica de Canarias, 38205 La Laguna, Tenerife, Spain
[4] Departamento de Astrofísica, Universidad de La Laguna, 38206 La Laguna, Tenerife, Spain
[5] Observatório do Valongo, Universidade Federal do Rio de Janeiro, Ladeira Pedro Antonio 43, 20080-090 Rio de Janeiro, Brazil
[6] School of Physics and Astronomy, Cardiff University, Queen's Buildings, The Parade, Cardiff CF24 3AA, UK
[7] Instituto de Física e Química, Universidade Federal de Itajuba, Av. BPS 1303-Pinheirinho, 37500-903 Ítajuba, Brazil
[8] Observatorio Astronómico de Córdoba, Universidad Nacional de Córdoba, Laprida 854, Córdoba, Argentina
[9] Laboratório Nacional de Astrofísica, Rua dos Estados Unidos, 154, Bairro das Nações, Itajubá, MG 37504-365, Brazil
[10] Leiden Observatory, Leiden University, PO Box 9513, 2300 RA Leiden, The Netherlands

Received 30 December 2024 / Accepted 19 March 2025

ABSTRACT

Context. We investigate the physico-chemical properties of the planetary nebula (PN) NGC 3242 in both 1D and 2D, using integral field unit (IFU) data. This PN has a complex morphology with multiple shells and contains a pair of structures with a lower degree of ionization compared to the main nebular components. The origin of these so-called low-ionization structures (LISs) remains a mystery.
Aims. With the capabilities offered by IFU spectroscopy, we aim to gain a better understanding of the behavior of nebular properties in the LISs and examine the spatial distribution of physico-chemical parameters in NGC 3242.
Methods. Data from the Multi Unit Spectroscopic Explorer (MUSE) at the Very Large Telescope (VLT) were used in order to perform a spatially resolved physico-chemical analysis of NGC 3242. The analysis was performed both in 2D, based on emission line maps, as well as in 1D, via simulations of long-slit spectroscopy, with pseudo-slits.
Results. Through the deeper investigation of MUSE data, we detected new structures perpendicular to the pair of LISs of NGC 3242, which are mainly seen in the light of [S III] and [N II]. In addition, two arc-like structures were revealed. Moreover, an inner jet-like structure was found through its [Fe III] emission. The interaction of the jet with the rim may be related to the formation of knots and blobs. The higher value of T_e, is estimated from the [S III] diagnostic lines, followed by T_e ([N II]), T_e(H I) and, finally, T_e (He I). In all cases, T_e is higher at the inner nebular structures. Regarding electron density, n_e, is lower at the LISs, while an increase is observed at the nebular rim. Diagnostic diagrams confirm that NGC 3242 is a highly ionized nebula. Moreover, for the first time, the MUSE data have unveiled the atomic line [C I] λ8727 in this PN, which is primarily emitted from the LISs. This finding suggests that these structures may consist of a molecular core surrounded by neutral and ionized gas.

Key words. techniques: imaging spectroscopy – ISM: abundances – dust, extinction – planetary nebulae: general – planetary nebulae: individual: NGC 3242

1. Introduction

As low- to intermediate-mass stars reach the end of their lives, their strong stellar winds become active, leading to the formation of an ionized gas region known as the planetary nebula (PN). The complicated morphology of PNe observed in most cases (e.g., irregular, point symmetric, asymmetric, and bipolar) cannot be explained from the generalized interacting stellar wind (ISW) model (Balick 1987; Icke 1988). Therefore, a number of studies have proposed different scenarios regarding their formation mechanisms (see Balick & Frank 2002, for a review). The main morphological structures of PNe include: the bright rim, shells, and halo. In addition, "rings" have been identified embedded in the halos of some PNe caused by different episodes of mass loss during the asymptotic giant branch (AGB) phase (Corradi et al. 2003).

Another open question in the study of PNe is the formation of small-scale structures with a lower ionization degree compared to the surrounding gas. These structures are known as low ionization structures (LISs), as the lines emitted from them are mainly low ionization ones such as [N II], [S II], and [O I] (Corradi et al. 1996; Balick et al. 1998; Gonçalves et al. 2001; Akras & Gonçalves 2016; Mari et al. 2023a). These LISs are classified according to their morphology as knots, filaments, jets, and jet-like systems (Gonçalves et al. 2001). Additionally, they are further divided into slow-moving low-ionization emitting regions, known as SLOWERS (Perinotto 2000), and fast low-ionization emission regions, known as FLIERS (Balick et al. 1993). The first category consists of LISs with radial velocities that are similar to the other nebular structures (e.g., NGC 7662, K 1-2, and Wray 17-1), while the second one includes those with velocities of ±25 km s^{-1} (or even higher in some cases Balick et al. 1993) with respect to their surrounding gas (e.g., NGC 3242, NGC 7009, and NGC 6543). Both the nature and the mechanisms that led to the formation of LISs, are not fully understood. Several scenarios have been proposed to explain their origin, but none of them seem to cover all types of LISs.

⋆ Corresponding author; lydiakonst@gmail.com

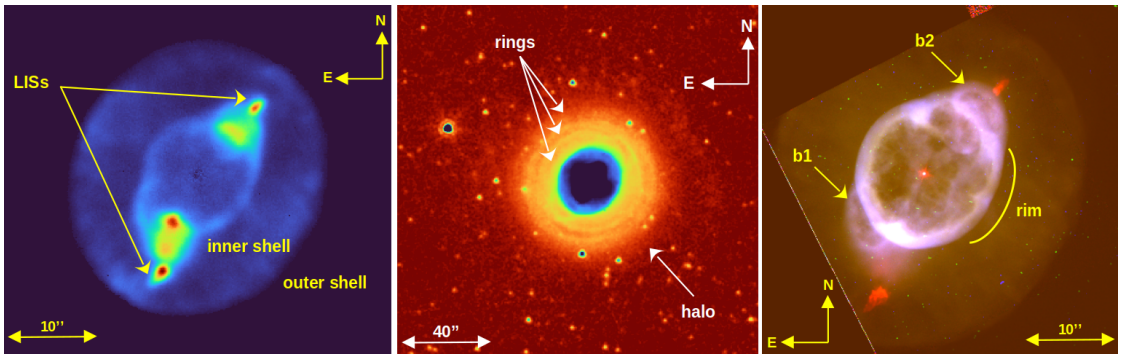

Fig. 1. Structures of NGC 3242. The left panel shows the [N II] λ6584 map from MUSE datacubes where the LISs and the nebular inner and outer shells are indicated. The middle panel illustrates the ratio 8.0/4.5 of IRAC bands, where three rings and the halo are visible. The final figure is an RGB image (R: [N II] λ6584, G: Hα, B: [O III] λ5007) from HST data, which shows the rim and the blobs.

Here, we investigate the spatial distribution of the physico-chemical properties of NGC 3242, with a main focus on its LISs. To this end, MUSE data are employed in conjunction with the SATELLITE code, developed by Akras et al. (2022a,b). NGC 3242, also known as Ghost of Jupiter, is located approximately 1279^{+63}_{-62} pc away, as it was estimated from Gaia mission (Bailer-Jones et al. 2021). Its central star (CS) has an effective temperature of ~80 000 K and a radius of 0.14 $R_\odot$ (Pottasch & Bernard-Salas 2008). As for its physico-chemical properties, the electron temperature (T_e) is around 11 000 K calculated either from [O III] or [N II] emission line ratios, while the electron density (n_e) is about 10^3 cm^{-3} based on [S II] and [Cl III] emission line ratios (Balick et al. 1993; Monreal-Ibero et al. 2005; Krabbe & Copetti 2005; Pottasch & Bernard-Salas 2008; Monteiro et al. 2013; Miller et al. 2016; Pottasch & Bernard-Salas 2008).

In terms of morphology, NGC 3242 is a multiple shell PN that contains a pair of LISs. Its inner shell is elliptical with size 28″×20″ and contains the rim, while the outer shell is 46″× 40″ and almost elliptical (Monteiro et al. 2013). In addition to the inner large scale structures, microstructures are also identified in the form of blobs and LISs. More specifically, two blobs (b1 and b2 in Fig. 1 from Gómez-Muñoz et al. 2015) are resolved NW and SE from the CS, respectively, while the LISs, also identified as FLIERS, appear between the two shells (Meaburn et al. 2000; Gómez-Muñoz et al. 2015), along the NW-SE orientation (Corradi et al. 2003). The velocities of the SE and the NW LISs are 22 and −28 km s^{-1} (relative to the systemic velocity, Vsys = (–6.6±1) km s^{-1}), respectively, estimated from high resolution spectra obtained with the Manchester Echelle Spectrograph (MES, see Gómez-Muñoz et al. 2015). The external shell is further surrounded by an extended halo. The latter is identified as a circular or slightly elliptical AGB halo, representing the final product of the thermal pulses at the end of the AGB phase (Corradi et al. 2003). At least three ring-like structures are observed within this halo via Hubble Space Telescope (HST) and Spitzer Space Telescope data (Gómez-Muñoz et al. 2015; Monreal-Ibero et al. 2005; Phillips et al. 2009). In addition, another extended ionized halo has been identified surrounding the first one (Corradi et al. 2003). Mid-infrared image data from the InfraRed Array Camera (IRAC) on Spitzer revealed that the external halo is also clumpy, possibly due to its fragmentation through Rayleigh-Taylor instabilities (Ramos-Larios & Phillips 2009). The aforementioned structures of NGC 3242 are illustrated in Fig. 1. More precisely, the left-panel of Fig. 1 shows the emission map of [N II] λ6584 (see Sect. 2, for details), labelling the nebular shells and the pair of LISs of NGC 3242. The middle and right panels were created using archival data from the Spitzer Space Telescope (programme: 1427, PI: calibration IRS) and the HST (programme: 6117, PI: Balick). The middle panel represents the ratio 8.0/4.5 of the Spitzer's Infrared Array Camera (IRAC) bands. In the same image, the outer nebular structures are indicated (rings and halo) in the wider field of view of the instrument (5.2′×5.2′). Finally, an RGB image was created resulting from the combination of [N II]: F658N (red), Hα: F656N (green), [O III]: F502N (blue) filters available on Wide Field Planetary Camera 2 (WFPC2) of HST. In this final panel, the rim and the blobs are labelled.

A number of studies have investigated the variations in the physical and chemical properties throughout PNe, placing a particular focus in their LISs, for instance, in the works of Hajian et al. (1997); Balick et al. (1998); Gonçalves et al. (2001); Gonçalves et al. (2009); Akras & Gonçalves (2016); Mari et al. (2023a,b). According to these studies, there is no significant variation in T_e between the main nebula and the LISs. On the contrary, n_e seems to decrease at the position of the LISs. This is the opposite result of what is expected from the theoretical scenarios on their formation, which predict that LISs should be denser than their surrounding environment (Steffen et al. 2001; Raga et al. 2008; Balick et al. 2020). A possible explanation for this disagreement is that LISs contain a molecular gas component, which is not considered when n_e is computed. Indeed, observations in several PNe have revealed the existence of molecular hydrogen in LISs (e.g., Fang et al. 2015, 2018; Akras et al. 2017; Akras et al. 2020a) and in the recently discovered clumps of NGC 3587 by Ramos-Larios et al. (2023).

In Sect. 2, we describe our approach and methodology. The results from the 1D and 2D analysis are presented in Sect. 3. In Sect. 4, we discuss our results and in Sect. 5 we summarize the main conclusions of this study.

2. Methodology

Integral Field Spectroscopy (IFS) offers the unique opportunity of simultaneously producing spatially resolved spectrum in two dimensions. In terms of PNe studies, this approach offers valuable insights into the spatial distribution of the emitted nebular spectra. NGC 3242 was first studied with the Integral field unit (IFU) Visible Multi-Object Spectrograph (VIMOS) by Monreal-Ibero et al. (2005) and some properties of its halo were identified. Later, Monteiro et al. (2013) used data from the same instrument for a more extended investigation of the

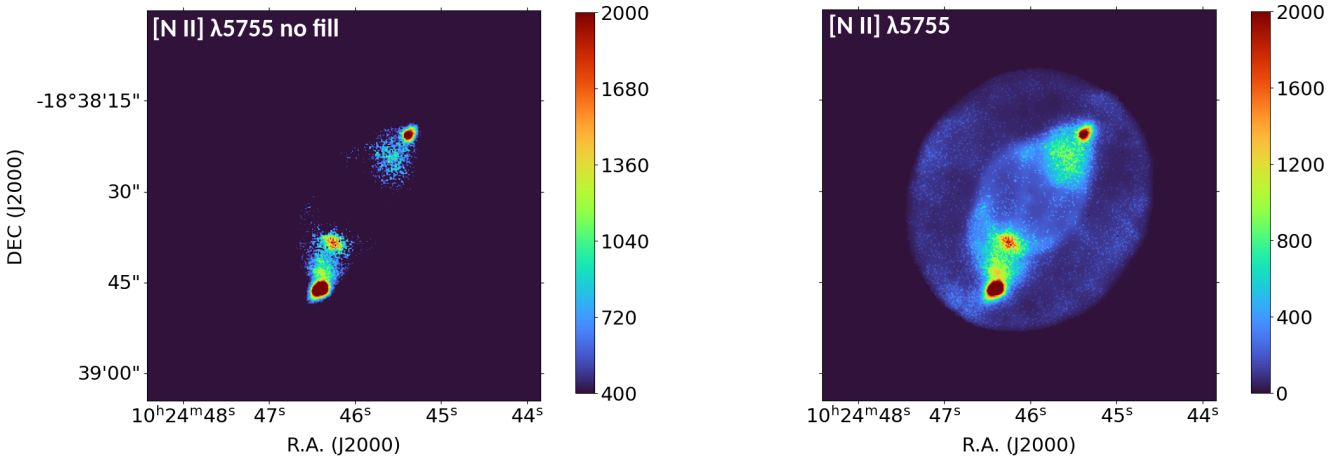

Fig. 2. Emission line maps of [N II] λ5755. The left panel illustrates the map after masking the pixels with low S/N, while in the right one is the final map that we used. The color bar represents pixel values (in terms of flux units $\times 10^{-20}$ erg s^{-1} cm^{-2} spaxel^{-1}).

Table 1. Observing log of the MUSE observations.

UT Start	n	Exp (s)	Airm.	Seeing (″)
Target: NGC 3242	Mode: WFM–NOAO-N			
2016-07-06 23:31:26.133	1/9	10.0	1.50	2.0
2016-07-06 23:33:35.638	2/9	60.0	1.50	1.5
2016-07-06 23:36:52.233	3/9	180.0	1.53	1.5
2016-07-06 23:41:23.196	4/9 [(a)]	60.0	1.55	1.0
2016-07-06 23:44:32.674	5/9	180.0	1.58	0.9
2016-07-06 23:49:29.663	6/9	180.0	1.62	1.1
2016-07-06 23:54:00.244	7/9 [(a)]	60.0	1.65	1.2
2016-07-06 23:57:09.890	8/9	180.0	1.69	1.2
2016-07-07 00:02:05.466	9/9	180.0	1.73	1.0

Notes. [(a)]Sky frames were taken 5 arcmin away from the object to ensure that there was no nebular contamination.

physico-chemical properties of this PN. In this work, archival data from MUSE IFU are used to perform a spectroscopic characterization of NGC 3242 (programme: 097.D-0241(A), PI: Corradi R.L.M.). MUSE has a wider field of view and better spectral and spatial resolution than VIMOS. In its nominal Wide-Field Mode (WFM-NOAO-N), MUSE covers a wavelength range from 480 to 930 nm, with a field of view of 1′× 1′, and a pixel scale of 0.2″ per pixel. Details on the reduction steps of the data can be found in García-Rojas et al. (2022). Table 1 summarizes the log of observations. For our analysis, two data cubes were used: one with an exposure time of 10 s and a deeper one with a total exposure time of 900 s. From these datacubes, we extracted emission line maps of some optical emission lines, typically observed in PNe and the error maps as produced by the fitting. All the fluxes and the associated errors were measured as described in Sect. 3 of García-Rojas et al. (2022). The brightest emission lines (Hα, Hβ, and [O III] $\lambda\lambda$4959, 5007) maps were extracted from the 10 s datacube, as they are saturated in the longer exposure datacube. Overall, 23 emission line maps were extracted from MUSE datacubes. In Table A.1, the observed and de-reddened line fluxes are listed, integrated from the whole PN (see the pseudo-slit dimension on the same table).

2.1. Masking on the emission maps

To exclude pixels with a low low signal-to-noise ratio (S/N), a mask was applied considering F(Hβ) > 0.002 × F(Hβ)$_{max}$, where F(Hβ)$_{max}$ is the maximum intensity of Hβ. A similar mask, but with 5% of F(Hβ)$_{max}$, was applied by García-Rojas et al. (2022). The lower limit was chosen because the LISs are relatively faint in Hβ compared to the rest of the nebula.

In some nebular regions, T_e ([N II]) was unrealistic, due to the low S/N in the measurement of the [N II] λ5755 line flux. Thus, in addition to the previous criterion, another mask was applied to the already corrected for recombination contribution [N II] λ5755 diagnostic line map (Sect. 3.8.1) to exclude pixel values with low S/N. To this end, the pixels where the ratio of the emission line map to the error map fell below 5, were set equal to zero (see Fig. 2, left panel). Then, the zero values in the [N II] λ5755 emission map were replaced so the temperature diagnostic ratio [N II] ((6548+6584)/5755) remains constant, producing a 2D map with constant T_e = 11 400 K (see Fig. 2, right panel). This T_e represents the mean value of the electron temperature at the LISs, where the [N II] λ5755 emission line has the higher S/N. We consider this a reasonable approximation, as previous 2D studies of NGC 3242 found no significant variation in T_e[N II] across different nebular regions (Monteiro et al. 2013).

2.2. SATELLITE code

We used the SATELLITE code (Akras et al. 2022a,b) to perform the spectroscopic analysis of NGC 3242 MUSE data. This code uses IFU data to carry out in-depth spectroscopic characterization of ionized nebulae (PNe, H II regions, or star forming galaxies). SATELLITE code has four modules: specific slit analysis, rotational analysis, radial analysis, and 2D analysis tasks. SATELLITE makes use of PyNeb (version 1.1.18, Luridiana et al. 2015; Morisset et al. 2020) and the atomic data available to compute the physical and chemical properties of the gas. The atomic data that were employed in this study are listed in Table 2. The emission lines are corrected for extinction, using PyNeb, by comparing the estimated ratio Hα/Hβ with the theoretical one (Hα/Hβ=2.86 in the low density limit for T_e=10 000 K, Osterbrock 1989; Storey & Hummer 1995). The interstellar extinction law (R$_v$) is a free parameter in SATELLITE and for the purposes of this study, we employed R$_v$ = 3.1 (Seaton 1979;

Table 2. Atomic data for CELs and ORLs.

Ion	Transition probabilities	Collision strengths
CELs		
O^0	Wiese et al. (1996)	Bhatia & Kastner (1995)
O^+	Zeippen (1982)	Kisielius et al. (2009)
	Wiese et al. (1996)	
O^{2+}	Storey & Zeippen (2000)	Storey et al. (2014)
	Froese Fischer & Tachiev (2004)	
N^0	Kaufman & Sugar (1986)	Pequignot & Aldrovandi (1976)
	Wiese et al. (1996)	Dopita et al. (1976)
N^+	Froese Fischer & Tachiev (2004)	Tayal (2011)
S^+	Rynkun et al. (2019)	Tayal & Zatsarinny (2010)
S^{2+}	Froese Fischer et al. (2006)	Tayal & Gupta (1999)
Cl^{2+}	Rynkun et al. (2019)	Butler & Zeippen (1989)
Ar^{2+}	Munoz Burgos et al. (2009)	Munoz Burgos et al. (2009)
ORLs		
Effective recombination coefficients		
H^+	Storey & Hummer (1995)	
He^+	Porter et al. (2012, 2013)	
He^{2+}	Storey & Hummer (1995)	

Howarth & Wilson 1983; Cardelli et al. 1989). Then the nebular physical parameters such as T_e and n_e, as well as the chemical parameters, such as ionic abundances, ionization correction factors (ICFs), total elemental abundances, and abundance ratios can be calculated using any of these modules. The uncertainties of the physico-chemical parameters in the 1D analysis were estimated based on 100 Monte Carlo simulations[1]. For each line intensity, random values are generated, using a Gaussian distribution centered on the observed line intensity with a standard deviation equal to its uncertainty. The code uses 35 emission lines, including the 23 lines that are the object of this study, both optical recombination lines (ORLs) and collisionally excited lines (CELs) that are typically observed in ionized nebulae. SATELLITE can conduct both 1D and 2D analyses, where in the first case, a number of pseudo-slits is used to simulate slit spectroscopy. Hence, this offers the opportunity of comparing results from IFS with previous studies that have been conducted using long-slit observations.

In the case of the specific slit analysis task, a default number of ten pseudo-slits is used for the spectroscopic characterization of the areas defined by them. This module can be used for the study of specific morphological nebular components. Regarding the rotational analysis, a number of pseudo-slits are simulated in different position angles (PA) from 0 to 360 degrees, while in the radial analysis module, a pseudo-slit is used to test the variation of nebular parameters with the distance from the CS. SATELLITE also performs the spectroscopic analysis in two spatial dimensions and the main results of this analysis are 2D maps of the nebular physical parameters. At the same time, emission line diagnostics are provided to better distinguish the excitation mechanisms occurring in different PNe structures. More detailed information on the modules and the spectroscopic analysis that SATELLITE code performs is available in Akras et al. (2022a,b).

[1] The errors remain almost invariant, even for a much higher number of Monte Carlo simulations. Thus, 100 iterations were chosen to achieve a balance between accurate uncertainties and computational runtime (see Delgado-Inglada et al. 2016; García-Rojas et al. 2022; Gómez-Llanos et al. 2024).

3. Results

3.1. The low-ionization structures

In the top-left panel of Fig. 3, we present the [N II] λ6584 emission line map. The bright rim and the pair of LISs are prominent in this map. They appear at position angles 160° and 320°, while their distances from the CS are 13″ and 16″, respectively. A single knot can also be identified near the nebular rim, at a distance of 8″ from the central star, while the [O III] emission line map (top-right panel) reveals a knot at PA = 12° and distance 7″ from the CS (k2 and k3 in Fig. 1, respectively). Gómez-Muñoz et al. (2015) first identified these knots via imaging with the Harold Johnson Telescope at the San Pedro Mártir Observatory (OAN-SPM). In the same study, a fifth knot was found, named as k4b. However, in the MUSE data, this knot has not been identified. For consistency, knots are marked with the same labels as in the previous work by Gómez-Muñoz et al. (2015).

Using the specific slit analysis module, we investigated the physical properties of the knots. For this analysis, four pseudo-slits were placed at the positions of the southeast (SE) and northwest (NW) LISs, hereafter referred to as k1 and k4, as well as at the positions of knots k2 and k3 (see the top panels of Fig. 3). In particular, T_e, n_e, and a few typical emission line ratios are presented in Fig. 4 and Table A.2. Emission line ratios, such as log([S III]/[S II]) and log([O III]/[O I]) (Mari et al. 2023a), provide key information on the ionization level of nebular structures. In the case of k1 and k4, the sum of [S II] emission lines is approximately twice as bright as the sum of [S III] lines, with log([S III] (9069+6312)/[S II] (6716+6731)) values of 0.37 and 0.58, respectively. In contrast, k2 and k3 appear to have higher values for the same ratio than the pair of LISs, both around 1. A similar trend is observed for log([O III] (4959+5007)/[O I] (6300+6363)), with the ratio being about two orders of magnitude higher in k2 and k3 compared to k1 and k4. This indicates that knots k2 and k3 are more prominent in high-ionization species, such as S^{2+} and O^{2+}, while low-ionization species dominate the emission in k1 and k4.

Moreover, log([N II] (6548+6584)/Hα) is almost one order of magnitude higher in k1 and k4 compared to k2 and k3. However, both k2 and k3 appear to be part of the rim, which could influence the estimated flux of low-ionization species. Since we cannot entirely rule out the rim's contribution, it remains possible that k2 and k3 share characteristics with other low-ionization features. Furthermore, n_e ([S II]) is higher in k2 and k3, with mean values ~4500 and ~3400 cm^{-3}, respectively. Since these structures seem to be parts of the nebular rim, we compare our estimations with the rim's n_e. The density values of the rim close to k2 are ~3500 cm^{-3}. This suggests that n_e in k2 is around 1000 cm^{-3} above the rim density. However, it has to be noted that the errors in the estimation of n_e are high. On the contrary, in the case of k3, n_e values conform to the electron density of the surrounding part of the rim.

In the case of T_e ([S III]), k3 is around 2000 K hotter than the other knots, which show a nearly constant T_e ([S III])~12 000 K. On the other hand, T_e ([N II]) is ~11 400 K for k1 and k4, while k2 and k3 exhibit 10 700 K and 11 400 K, respectively (Fig. 4 and Table A.2). However, it should be noted that at the position of k2 and k3, [N II] λ5755 emission line is contaminated by recombination, affecting T_e ([N II]) at these regions (see Sect. 3.8.1). Gómez-Muñoz et al. (2015) suggested that even if T_e is not significantly higher at k2 and k3, these lines could still have been created from shock material. Here, we propose they are likely to

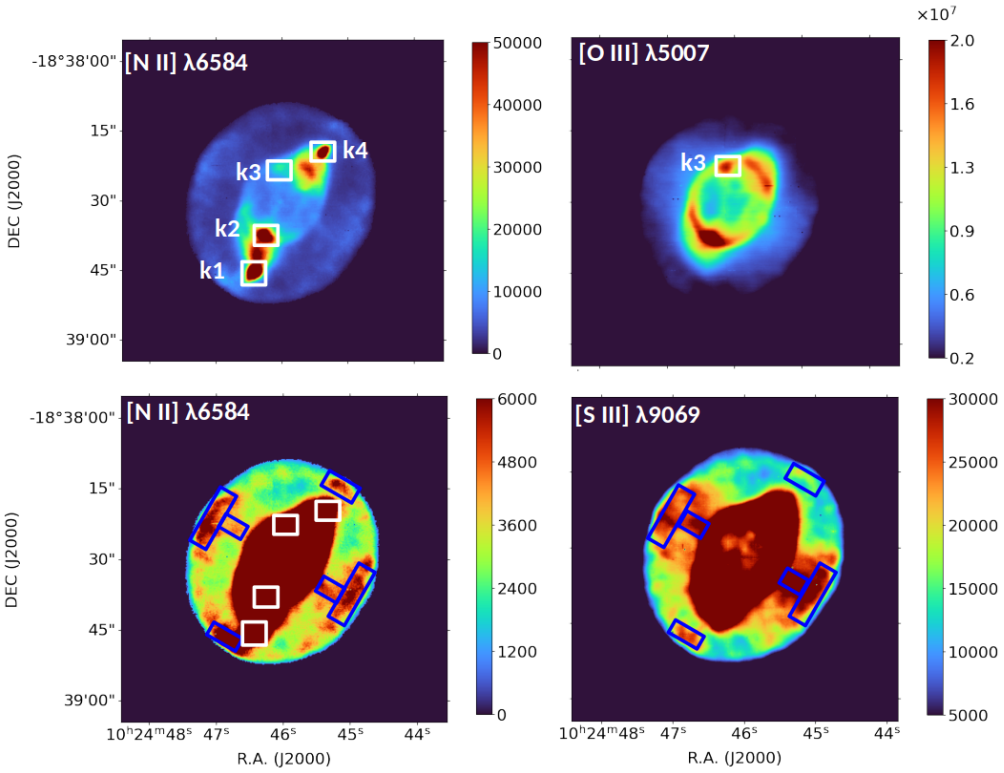

Fig. 3. Emission line maps of [N II] λ6584 (top left and bottom left), [O III] λ5007 (top right), and [S III] λ9069 (bottom right) for NGC 3242. In the top panels, the four knots are marked. The bottom high-contrast images show the new structures at the nebular shell (blue rectangles), while in the bottom-left, the four knots are marked as well (white rectangles). The color bar represent flux values (in units of $\times 10^{-20}$ erg s^{-1} cm^{-2} spaxel^{-1}).

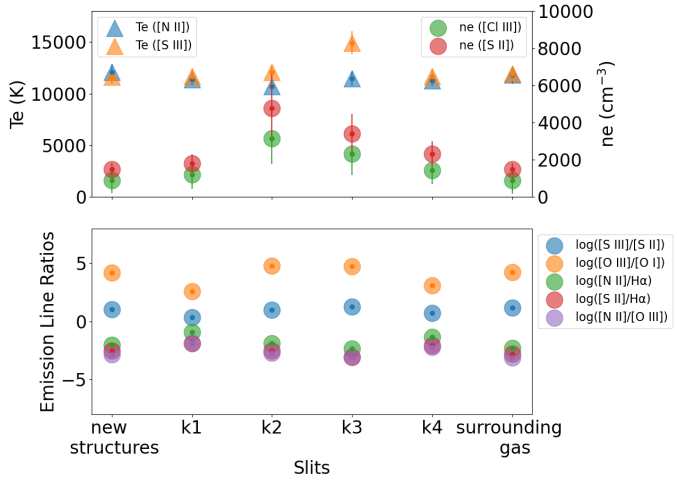

Fig. 4. Top: T_e and n_e for the different structures listed in Table A.2. Bottom: some emission line ratios for the same structures. In several cases, the error-bars are smaller than the symbols (see Table A.2).

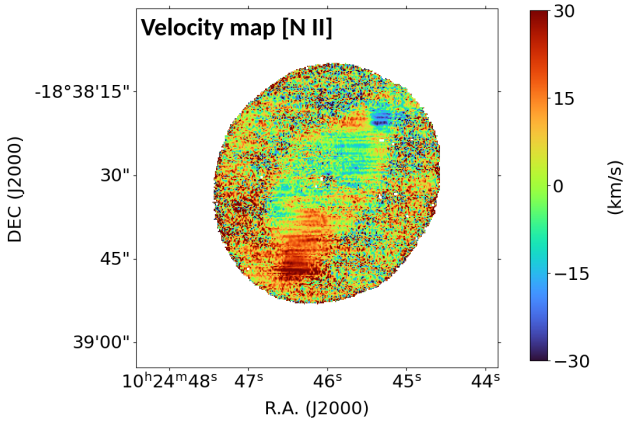

Fig. 5. Velocity map from [N II] λ6584 emission line. The color bar displays absolute velocities.

be the result of a dynamic interaction at the rim, caused by an inner jet (see Sect. 3.3).

In addition, 2D velocity maps were constructed based on [N II] emission lines to examine the kinematics of the LISs. The resolution of MUSE is not sufficient for a thorough kinematic analysis and the errors of the estimated velocities are high (~60 km s^{-1}), but we can still gain valuable insights into the nebular dynamics of NGC 3242 from the 2D velocity maps. Based on the velocity map shown in Fig. 5, k4 is blue-shifted, while k1 is red-shifted, with a relative velocity difference of 60 km s^{-1} between them.

3.2. Atomic gas and first detection of the far-red [C I] λ8727

Many studies thus far have revealed the presence of atomic carbon lines such as [C I] $\lambda\lambda\lambda$8727, 9824, and 9850 in PNe, (see Table 1 in Akras et al. 2024, and references therein). However, the majority of these studies were conducted using long-slit spectroscopy, making it unclear which specific nebular region predominantly emits these lines. In this context, the investigation of MUSE data for NGC 3242 revealed the presence of the far-red atomic [C I] λ8727 emission line, mainly emitted from its LISs, with a flux of around 2.5 $\times$ 10^{-16} erg s^{-1} cm^{-2} in both sides. The left panel of Fig. 6 shows the [C I] λ8727 emission line map. Recently, the same far-red [C I] emission line was detected in the LISs of NGC 7009 using MUSE data

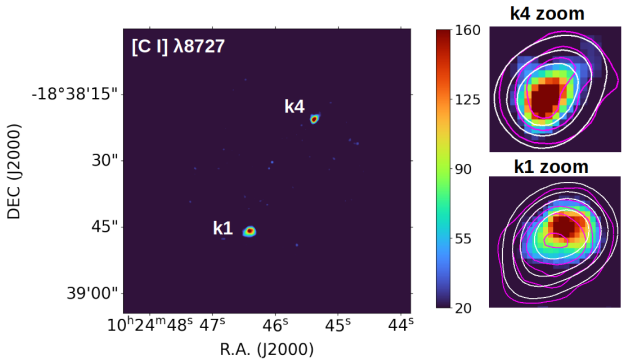

Fig. 6. Detection of [C I] λ8727 at k1 and k4 LISs. The zoomed in figures show also the contours for the [O I] λ6300 (white) and [N I] $\lambda\lambda$5198,5200 (magenta) emission lines. The images are smoothed with σ = 1.5. The color bar represents the values of the pixels (in flux units $\times 10^{-20}$ erg s^{-1} cm^{-2} spaxel^{-1}).

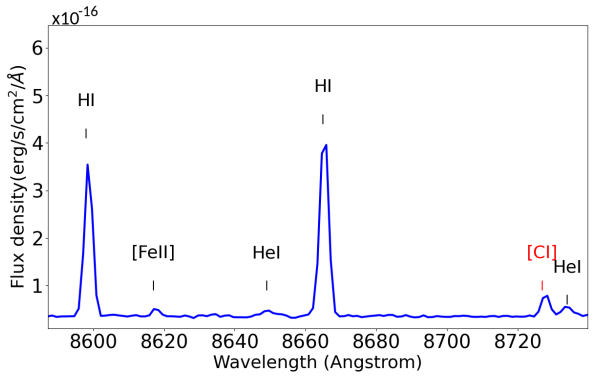

Fig. 7. Extracted spectrum from MUSE datacube in the region of k1. The [C I] λ8727 emission line is marked with red color. The [Fe II] λ8617 emission line is also identified in the spectrum.

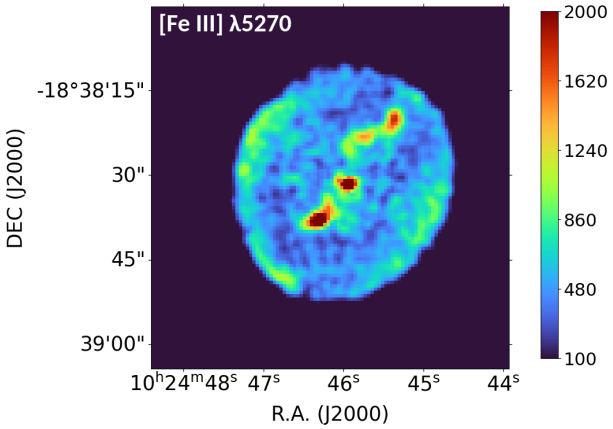

Fig. 8. [Fe III] λ5270 emission line map. The map is scaled down 3 times and smoothed with a σ=1. The color bar represents the values of the pixels (in flux units $\times 10^{-20}$ erg s^{-1} cm^{-2} spaxel^{-1}).

(Akras et al. 2024). The detection of [C I] emission in LISs, along with the enhanced emission of low-ionization lines such as [N II], [S II], [O I] supports the idea that LISs are potential mini-photo-dissociation regions (PDRs) embedded in PNe (Aleman et al. 2011). After all, the [C I] λ8727 line has already been detected in PDRs within H II regions, (see Henney & Valerdi 2024, and references therein).

The atomic gas of the LISs is also characterized by the emission of [O I] and [N I] lines (see theoretical work from Aleman et al. 2011). Here, the [N I] $\lambda\lambda$5198, 5200 doublet was found to emanate from the LISs of NGC 3242 with a mean flux, between k1 and k4, of 2.3 $\times$ 10^{-15} erg s^{-1} cm^{-2}, while [O I] $\lambda\lambda$6300, 6363 emission lines were detected with mean fluxes, between k1 and k4, 4.1 $\times$ 10^{-14} and 1.3 $\times$ 10^{-14} erg s^{-1} cm^{-2}, respectively. The line fluxes for the aforementioned atomic lines were estimated in a region of 5″ $\times$ 4″ centered at k1 or k4 (see Fig. 3) The contours of [O I] λ6300 and [N I] $\lambda\lambda$5198, 5200 emission lines on the [C I] λ8727 map are presented in the right panels of Fig. 6. An overlap is observed between [O I] and [N I] while there is small offset with the emission of [C I] (better seen in the radial profiles presented in Sect. 3.4).

3.3. Iron emission in NGC 3242

A weak detection of [Fe II] λ8617 emission line can be seen in the spectrum of the k1 LIS (Figure 7). Generally, [Fe II] is considered as shock tracer and is usually detected in shock excited regions of gaseous nebulae such as SNRs (e.g., Temim et al. 2024) or Herbig–Haro objects (e.g., Reiter et al. 2019). In the case of NGC 3242, this emission is concentrated in the k1 and k4, which could indicate a shock origin for the LISs. A jet-like structure is also unveiled in the [Fe III] λ5270 emission line map, beginning close to the central star and pointing towards the direction of the LISs. The jet appears asymmetric with the northwest part, being more extended than the southeast part (see Fig. 8), due to the orientation of the nebula (Gómez-Muñoz et al. 2015).

3.4. Radial profiles of typical emission lines

The SATELLITE radial analysis module was used to examine how the surface brightness of typical emission lines changes with the distance from the CS and to detect the ionization stratification at the position of the LISs. Two different pseudo-slits were used, placed at position angles of 160° and 320° (from the north and counterclockwise). In each case, the pseudo-slit had dimensions 19″ $\times$ 2″, extending from the CS to the outer regions of the nebula. Knot k1 is located 13″ from the CS, while k4 is at a distance of 16″.

The intensities of moderate- and high-ionization lines of He II, [O III], and [S III] show peaks at distances closer to the CS and near the rim. In contrast, the low-ionization lines [S II], [N II], [Fe II], and the atomic lines of [C I] and [O I] show a prominent peak at the position of LISs (see Fig. 9). Also, [S II] exhibits a first pick at the rim. This is reasonable, since S^+ requires photon energies ~ 10.4 eV, which is lower than the ionization potential of N^+ (~ 14.5 eV). So, S^+ is created while N^+ is still shielded by hydrogen, leading to the emission from different regions. In general, no significant spatial offset is found between the low-ionization lines. In particular, all lines exhibit a peak at (16.0–16.2)″ and (13.2–13.6)″ along the direction of k1 and k4, respectively. Surprisingly, an offset of ~0.5″ is detected in [Fe II] compared to [C I] in both pseudo-slit directions (further analysis on this issue in Bouvis et al. in prep.). We note that MUSE's spatial sampling is 0.2″. Moreover, our results are well aligned with the ionization stratification found in the LISs of NGC 7009 by Akras et al. (2020a); Gonçalves et al. (2003).

On the contrary, the peak emission of moderate- and high-ionization lines exhibit different trend in both directions. Along the direction of k1 (PA of 160 degrees), He II line peaks first at 8.2″ from the CS and then the [O III] and [S III] lines peak further away, at ~9.2″. On the other hand, in the direction of k4

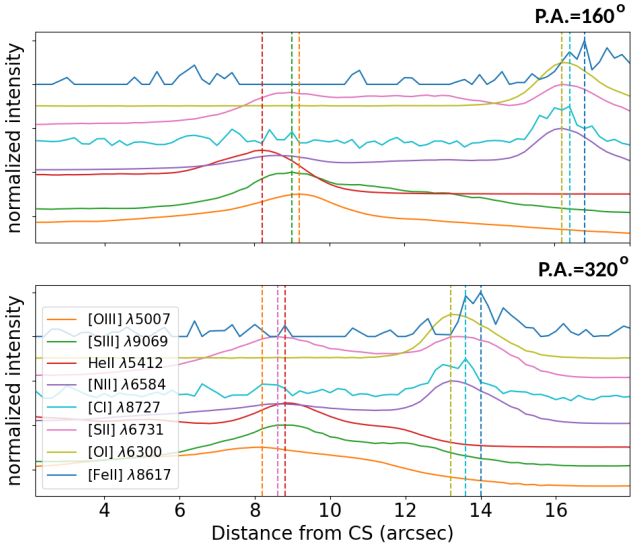

Fig. 9. Radial profiles of some typical optical emission lines for PA = 160° (top panel) and PA = 320° (bottom panel). The line intensities are normalized and an offset of 0.5 has been applied between the lines. The dashed lines define the pick intensities. There is an overlap in the picks of [N II], [S II] and [C I] for both PA and between [S III] and the first pick of [S II] only for PA=360°.

(PA 320 degrees) [O III] peaks at 8.2″ and then [S III] and He II follow at distances of 8.6″ and 8.8″ from the CS, respectively.

3.5. Nebular shell

Thanks to a detailed investigation of the NGC 3242 MUSE data, new structures were discovered perpendicular to the pair of LISs, extending from the nebular rim to the inner shell. The enhanced emission is mainly observed in the [S III] and [N II] emission line maps (see bottom panels in Fig. 3). Two faint arc-like structures are also visible above k1 and k4 at distances of 21″ and 19″ from the CS, respectively. The two arcs are radially symmetric with respect to the CS and are also aligned with k4 and k2, while an offset is observed in the case of k1 (see Fig. 3).

Six pseudo-slits were placed along the identified structures, shown as blue rectangles in the bottom panels of Fig. 3. The six regions defined by these pseudo-slits did not show significant differences among them. The mean values for their physical properties and some emission line ratios are presented in the second column of Table A.2. The bright structures at the leading edges of the nebular inner shell are more prominent in [S III] and [N II]. To our knowledge, this is the first time that these structures have been detected in NGC 3242. Moreover, [Fe III] emission has also been detected from the same structures (see Fig. 8). To assess whether these structures could result from shock interactions, the logarithmic ratios of [S II]/Hα and [N II]/Hα were examined (Sabbadin et al. 1977; Riesgo & López 2006; Leonidaki et al. 2013). We estimated mean values of log([S II] (6316+6731)/Hα) = −2.54 ± 0.03 and log([N II] (6548+6584)/Hα) = −2.04 ± 0.03, indicating that photoionization is likely to be the prevailing mechanism in these regions (Akras et al. 2020b). The electron temperature in these regions is T_e ([S III]) = (11 600 ± 660) K, while the electron density is n_e ([Cl III]) = (900 ± 500) cm^{-3}. Both T_e and n_e are consistent with the values estimated for the gas around the new structures (blue regions in the bottom panels of Fig. 3, see last column of Table A.2).

3.6. Electron temperature and electron density from CELs

The extinction coefficient c(Hβ), electron temperature (T_e), and density (n_e), are key parameters for the physical characterization of a nebula. Here, the rotational analysis module is employed to test the behavior of c(Hβ), T_e, and n_e with the position angle of a pseudo-slit. For this purpose, we considered pseudo-slits extending from the CS to the outer nebular regions, with the PA increasing in steps of 10° from 0° to 360°. In Fig. 11, we show the behavior of c(Hβ) (upper panel), T_e ([S III]) (middle panel), and n_e ([S II]) (lower panel), computed from the different pseudo-slits described above. We found that c(Hβ) is almost constant throughout the nebula, with a mean value of 0.140 ± 0.024. On the other hand, T_e ([S III]) also remains almost constant (between 14 000 K and 15 000 K) for most PA values, with a significant decrease of about 4000 K around PA 160° and 320°, which coincides with the orientations of the LISs. Furthermore, n_e ([S II]) is around 2000 cm^{-3} for most PA, but reaches higher values also in the direction of the LISs. It is important to note that these values do not necessarily imply an actual increase in n_e (or decrease in T_e) at the LISs, since the resulting T_e and n_e are the integrated values along the pseudo-slits. It is worth noticing, however, based on the radial analysis, it is evident that the position of the slit can yield to notable discrepancies in the T_e and n_e values. In the following paragraphs, we examine the 2D spatial distribution of both T_e and n_e, which provides further insight into what is occurring at the LISs.

In the T_e ([S III]) 2D map, presented in the upper right panel of Fig. 10, it is evident that T_e is higher at the nebular rim, where it reaches values of ∼17 000 K. This behavior has been previously observed in T_e ([O III]) (Balick et al. 1993; Monteiro et al. 2013) as well. The NW and SE parts of the rim are not as extended, and they do not significantly affect the integrated value of the electron temperature found through the rotational analysis. In contrast, along the minor nebular axis, the contribution of the rim to T_e is not negligible, resulting in higher values when the slit analysis is considered. The mean T_e ([S III]) from the 2D map is (12 500 ± 1700) K.

In the upper-left panel of Fig. 10, we also present the electron temperature calculated from the [N II] diagnostic lines. It is important to note that, due to the mask that we applied to the [N II] λ5755 line map (see Sect. 2.1), T_e ([N II]) is only well-defined in the unmasked regions of the nebula, which correspond to the lower ionization degree zones around the LISs. In this case, T_e ([N II]) has a mean value of (11 700 ± 1500) K, in good agreement with previous studies (Krabbe & Copetti 2006; Pottasch & Bernard-Salas 2008; Monteiro et al. 2013).

As for the electron density, we calculated a mean n_e ([S II]) of (2200 ± 1500) cm^{-3} and n_e ([Cl III]) of (1600 ± 1000) cm^{-3} from the 2D density maps (lower panels of Fig. 10), given T_e ([N II]) and T_e ([S III]), respectively. In both cases, the electron density of the LISs is lower than the surrounding nebula. The fact that LISs are less dense than the surrounding nebula is in conflict with the theoretical scenarios about their formation (e.g., Steffen et al. 2001; Raga et al. 2008). On the contrary, the highest values for n_e are observed at the nebular rim, which explains the increase that was previously noticed at PA 160° and 320° through the rotational analysis. The mean values, the median, the Q3 and 95% percentiles and the standard deviation for c(Hβ), T_e and n_e are also listed in Table 3.

3.7. Electron temperature from ORLs

Certain recombination lines can also be used for the estimation of T_e. Based on the He I 7281/6678 diagnostic ratio, T_e can be

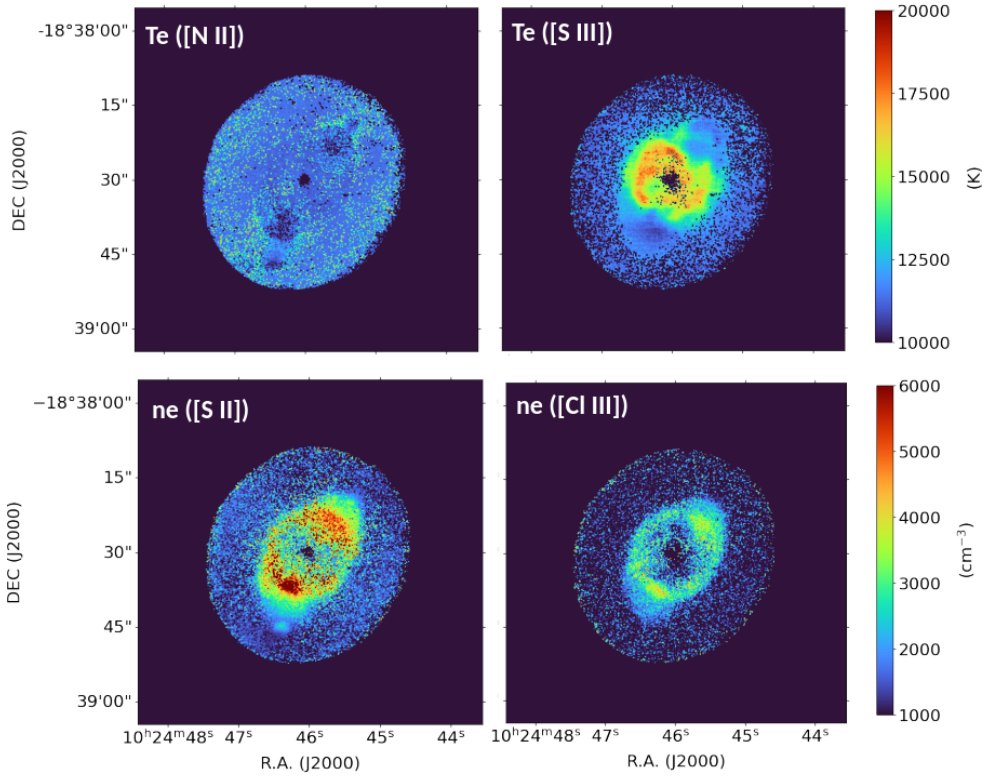

Fig. 10. Electron temperature and electron density 2D maps from CELs. T_e is calculated from [N II] and [S III] emission maps (top-left and right panels, respectively). n_e is calculated from [S II] and [Cl III] emission maps, assuming T_e ([N II]) and T_e ([S III]), respectively (bottom panel left and right, respectively).

Table 3. Median values, the 75% percentile (Q3), the 95% percentile, the mean and the standard deviation (σ) are presented for c(Hβ), T_e in K, and n_e in cm^{-3} of the entire PN.

	Median	Q3	95%	Mean	σ
c(Hβ)	0.14	0.18	0.24	0.14	0.06
T_e ([N II])	11 300	11 400	15 700	11 700	1500
T_e ([S III])	11 900	12 900	16 400	12 500	1700
T_e (He I)	5400	4000	7200	5700	2200
	7800 (†)	8300 (†)	9100 (†)	7800 (†)	1000 (†)
T_e (PJ)	8000	11 400	20 700	9300	5300
	9000 (†)	10 200 (†)	15 800 (†)	8900 (†)	3700 (†)
n_e ([S II])	1700	2600	4900	2200	1500
n_e ([Cl III])	1400	2200	3400	1600	1000

Notes. (†)T_e (PJ), T_e (He I), and σ, estimated in the elliptical annulus of Fig. 12.

estimated either by an analytic formula or by a linear representation. The latter approach is only valid in the low T_e regime (T_e<15 000 K). The analytic formula involves the corrected intensities of He I $\lambda\lambda$7281, 6678 lines and three fitting parameters: a_i, b_i, and c_i (see relation 1 from Zhang et al. 2005a), which are associated with the line emissivities. The fitting parameters were estimated following the procedure described by Benjamin et al. (1999), but using the most recent emissivities from (Porter et al. 2012, 2013) available in PyNeb (Luridiana et al. 2015; Morisset et al. 2020). These fitting parameters are also density dependent, so a_i, b_i, and c_i were first estimated for n_e values of 100, 1000, and 10 000 cm^{-3}. Then a minimization process was applied to refine them, given the n_e computed for NGC 3242.

In cases of T_e<15 000 K, a linear representation is sufficient to estimate T_e (He I). Zhang et al. (2005b), provided a linear representation for T_e with uncertainties up to 7% and without any dependencies on n_e. Similarly, Méndez-Delgado et al. (2021), provided another linear representation that varies with n_e at low densities, but remains constant at higher n_e values. This relationship involves the fitting parameters α and β, which were estimated from a linear interpolation of n_e values of NGC 3242 over the range of n_e provided in Table D7 of Méndez-Delgado et al. (2021). We applied each of these approaches and found that Zhang et al. (2005a) and Méndez-Delgado et al. (2021) are in good agreement for our case, with mean values of ~5650 K and ~6000 K, respectively. In contrast, the Zhang et al. (2005b) method tends to yield lower electron temperatures. The right panel of Fig. 12 shows an example of T_e (He I) map generated using the approach of Zhang et al. (2005a). Spatially, there is no significant variation among the inner nebular structures, although the rim exhibits a slightly higher temperature. The lowest T_e (He I) is observed at the nebular shell, where it reaches values around 4000 K. The mean value of T_e (He I) is 5700 K (Table 3), which is in good agreement with previous studies (Tsamis et al. 2003). It is also worth noticing that the He I λ7281 emission line is fainter in comparison with the He I λ6678 emission, affecting T_e (He I) and leading to lower values at the nebular outer shell. In a very recent paper, Méndez-Delgado et al. (2024) claimed that the lower T_e (He I) observed in photoionized nebulae relative to T_e ([O III]) can be explained by a combination of photon loss from He$^+$ $n^1P \rightarrow 1^1S$ transitions (deviations from "case B") and the effect of temperature inhomogeneities in the nebula. We discuss this further in Sect. 4.2.

The electron temperature can also be calculated from the ratio of the H I continuum Balmer jump (BJ) or Paschen jump

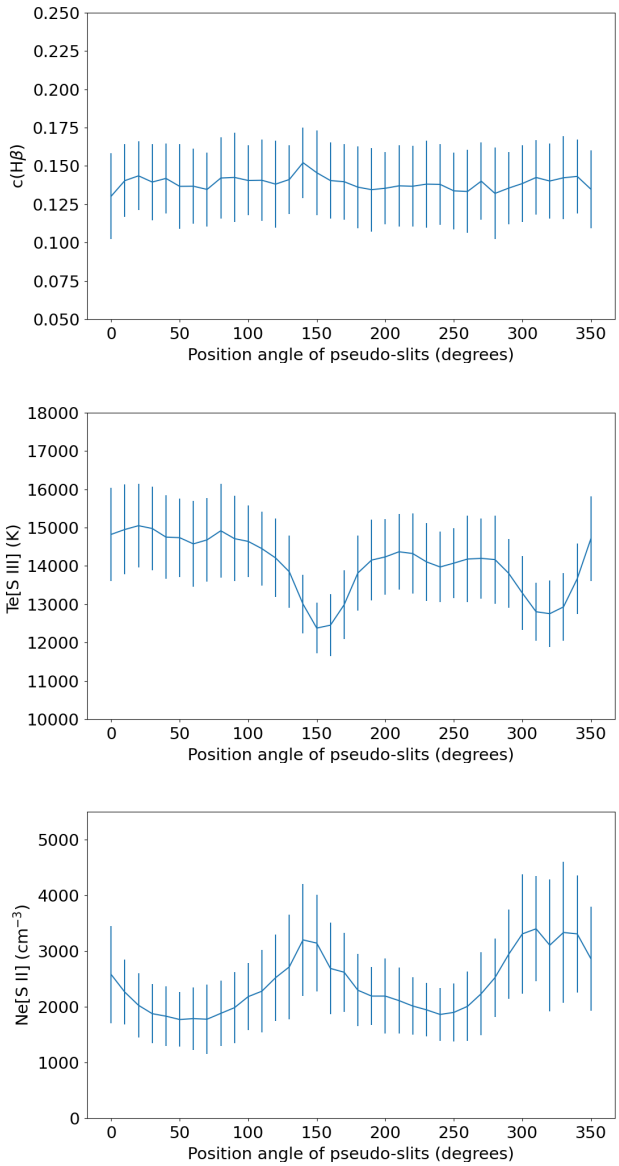

Fig. 11. Top to bottom: c(Hβ), T_e[S III] and n_e[S II] versus the PA of the pseudo-slit from 0° to 360°. The error-bars are estimated from 100 Monte Carlo iterations.

(PJ) at 3645 Å and 8200 Å, respectively, to a nearby H I line. In the MUSE wavelength range, only the Paschen jump is available. For the estimation of the continuum before and after the PJ, the Continuum class of PyNeb (Luridiana et al. 2015; Morisset et al. 2020) was used, assuming constant n_e =1.5 × 10^3 cm^{-3}, He^+/H^+ = 7.35 × 10^{-2}, and He^{2+}/H^+ = 2.24 × 10^{-2}. The continuum before and after the PJ was estimated at ~8100 Å and ~8400 Å, respectively, normalized to H I P9 emission line at 9229 Å. This line was chosen instead of P11, which is closer to the jump, because P11 is fainter, and we wanted to avoid the additional noise to the T_e (PJ) map. Then, we interpolated over the observed PJ, which was estimated by extracting continuum slices from the MUSE datacube, and normalizing them to the P9 emission line map. The 2D map that was constructed from this analysis is presented in the left panel of Fig. 12. At the outer nebular region, the temperature map is quite noisy and highly uncertain, probably due to the noisy continuum emission. The mean value is ~9300 K, which is in good agreement with the value that was previously estimated by Tsamis et al. (2003) for NGC 3242. Table 3, shows that the median T_e (He I) is around 4500 K lower than T_e (PJ), in very good agreement with what was observed by Zhang et al. (2005a) in a sample of PNe, where they found an average difference of T_e(H I)−T_e(He I) of approximately 4000 K. However, since both temperatures are not well defined outside the borders of the rim, the magnitude of this difference is weighted to the values obtained at the outer nebular regions. Thus, to properly compare them, we compared the median values in an ellipse containing the inner shell, but not the position of the central source (see Fig. 12). In this region, the median values of T_e (He I) and T_e (PJ) are (7800 ± 1000) K and (8900 ± 3700) K, respectively, which are now in better agreement than those estimated for the entire PN. We discuss this issue further in Sect. 4.2.

3.8. Ionic and total abundances

Theoretically, the elemental abundance of a given element is simply the sum of the abundances of all its ionic species present in the gas. However, this is not the case when only the optical range is studied, and ICF must be applied to account for the unobserved ions. In this study, we adopt the ICF approach proposed by Kingsburgh & Barlow (1994). SATELLITE also estimates the ICFs recommended by Delgado-Inglada et al. (2014), but since NGC 3242 is a high-excitation nebula, the criteria to estimate the ICFs from Delgado-Inglada et al. (2014) were not satisfied in many cases. Using the specific slit analysis module of SATELLITE and selecting a pseudo-slit that covers the entire nebula (centered at the center of the PN with dimensions 40″ × 50″), we performed an analysis of the integrated spectrum of NGC 3242. This allowed us to calculate the physical conditions and the ionic and elemental abundances, which were then compared to the results from previous studies. In Figs. B.1 and B.2, we present 2D ionic abundance maps for some species, along with the elemental abundance of He, which is the only element that does not require the use of an ICF. For the low ionization ions (e.g. N^+, S^+), the low excitation electron temperature T_e ([N II]) and density n_e ([S II]) were used to compute ionic abundances. For high-ionization ions, such as O^{2+}, Cl^{2+} or S^{2+}, T_e ([S III]), and n_e ([Cl III]) were employed. The second column of Table 4 presents the computed physical conditions, as well as the ionic and total abundances from the specific slit analysis.

In terms of spatial distribution, He/H does not vary significantly throughout the PN, but there is a visible trend toward higher values on the east side of the major axis (see Figs. B.1 and B.2). Regarding the He ions, we see that He^{2+}/H^+ is mainly concentrated in the inner nebular structures due to its higher ionization state, while He^+/H^+ is widely distributed throughout the PN. Furthermore, N^+/H^+, O^+/H^+ and S^+/H^+ are more abundant in the LISs, as expected (Figs. B.1 and B.2). In contrast, O^{2+}/H^+ exhibits high values across the nebular structures, which corresponds to strong [O III] emission, for instance, log([O III] (4959+5007)/Hβ) = 1.2.

3.8.1. Effect of possible recombination contribution to the chemical abundances

At this point, it is worth mentioning that both [N II] λ5755 auroral and [O II] $\lambda\lambda$7320,7330 transauroral lines are potentially affected by recombination emission (Liu et al. 2000). To correct the intensity of [N II] λ5755 auroral line from this effect, we used two different approaches. First, we use the recipe provided by Liu et al. (2000) in their Eq. (1). This approach is valid in the

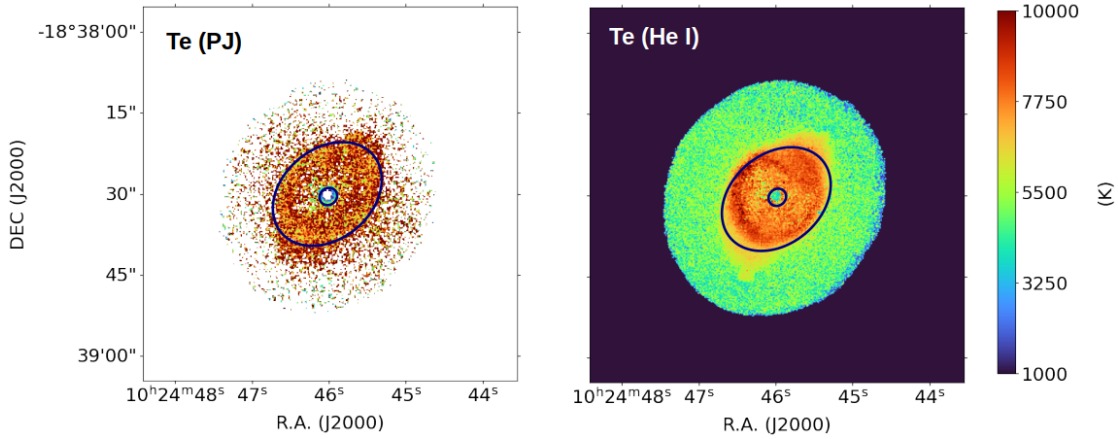

Fig. 12. Electron temperature maps from the ratio of the Paschen discontinuity to H I P9 line (T_e(PJ), left panel), and from the He I λ7281/λ6678 recombination line ratio (right panel). The blue ellipse marks the boundaries of the inner shell.

5000 K $\leq T_e \leq$ 20 000 K range, which is what we expect in PNe with low abundance discrepancy factors (ADF), as is the case for NGC 3242. Adopting T_e = 12 700 K and the N^{2+}/H^+ value obtained from the N II λ5679 recombination line, the recombination contribution is estimated to be ~30% for the integrated intensity of [N II] λ5755 (normalized to Hβ=100) in the entire PN (for pseudo-slit's dimensions see Table 4); however, this contribution is higher at the nebular rim (~40%). This is reasonable, since most of the N II λ5679 emission comes from the rim (see Fig. 13). This result agrees within the errors with the one of Tsamis et al. (2003) using the N^{2+}/H^+ from recombination lines.

Another way to account for the recombination contribution to the [N II] λ5755 line has been provided by García-Rojas et al. (2022):

$$I(5755)_{cor} = I(5755) - \frac{j_{5755}(T_e, n_e)}{j_{5679}(T_e, n_e)} \times I(5679), \quad (1)$$

where, j_{5755} and j_{5679} are the recombination emissivities. This approach was adopted by García-Rojas et al. (2022) to account for the recombination contribution in high-ADF PNe, where a cold plasma component (with a T_e value that is much lower than 5000 K) emits the bulk of metal recombination lines; hence, it is out of the validity range for the use of the Liu et al. (2000) formula. The flux of the N II λ5679 recombination line was extracted from the MUSE datacube and integrated for the entire nebula, while T_e = 12 700 K and n_e = 1600 cm^{-3} were adopted for the estimation of the recombination emissivities. As in García-Rojas et al. (2022), the recombination coefficients to compute the emissivities were adopted from Fang et al. (2011) and Pequignot et al. (1991) for the λ5679 and λ5755 recombination emission, respectively. Following this approach, the recombination contribution for [N II] λ5755 emission line is estimated to be ~30% of the observed intensity, almost identical to the correction obtained following the previous approach. These results seem to confirm the validity of the Liu et al. (2000)'s formula in the 5000 K $\leq T_e \leq$ 20 000 K range.

Moreover, an inspection of the spatial distribution of the N II λ5679 or C II λ6461 recombination lines in Fig. 13 shows that there is no recombination emission in the LISs, but only in zones that are internal to the rim. At the nebular rim, the corrected intensity of [N II] λ5755 is 0.05 (instead of 0.08), normalized to Hβ=100, while T_e ([N II]) is (10 900 ± 600) K instead of (12 900 ± 760) K, indicating a decrease of ~2000 K. The recombination correction was applied to the [N II] λ5755 emission line map, since both the N II λ5679 and [N II] λ5755 emission lines are intense at the nebular rim. Nonetheless, when estimating the chemical abundances of the PN, considering the mask applied to [N II] λ5755, the effect of the recombination contribution drops to ~4%. However, we accounted for this correction and re-estimated the ionic/total abundances of the nebula, which are listed in the first column of Table 4.

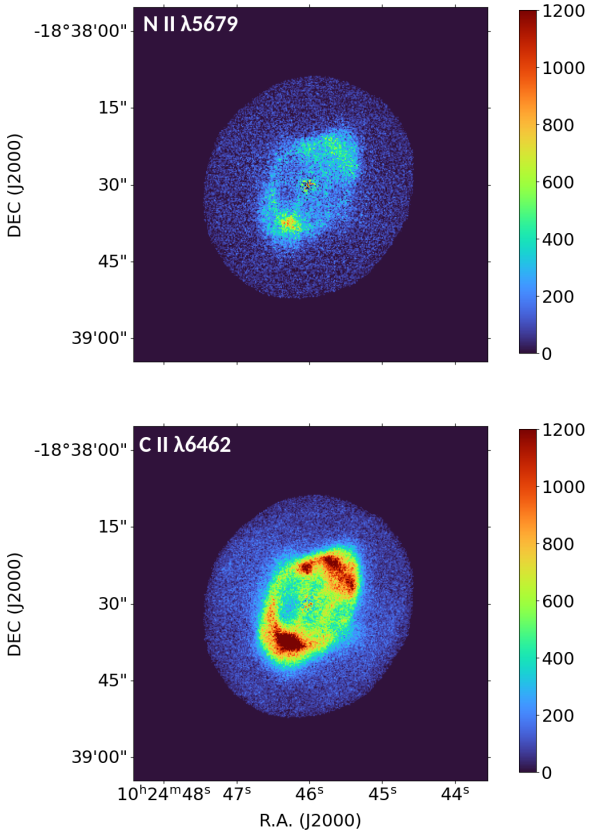

Fig. 13. N II λ5679 (top panel) and C II λ6462 (bottom panel) emission line maps. The color bar represents the values of the pixels (in flux units $\times 10^{-20}$ erg s^{-1} cm^{-2} spaxel^{-1}).

Regarding the [O II] $\lambda\lambda$7320,7330 lines, we could not adopt the approach by García-Rojas et al. (2022) because the nominal wavelength range used for our NGC 3242 MUSE data does not

Table 4. Integrated T_e, n_e, ionic and elemental abundances from this study in comparison with previous ones.

	Our study	MH16 (†††)	MG13	PB08	KC06	TS03
			T_e(K)/n_e (cm^{-3})			
T_e ([S III])	12 700 ± 800		–	–	–	–
T_e ([O III])	–	11 700 ± 300	12 900 ± 720	10 800	12 140 ± 31	11 700
T_e ([N II])	11 500 ± 600	–	11 670 ± 1000	11 000	–	13 400
n_e ([Cl III])	1600 ± 900	–	2380 ± 1300	3000	2531 ± 1227	1200
n_e ([S II])	2300 ± 700	–	3120 ± 1400	1900	1016 ± 436	1970
n_e (C II])	–	4500 ± 300	–	–	–	–
			Ionic and elemental abundances			
$He^+/H^+(\times10^{-2})$	7.35 ± 0.42	6.25 ± 0.45	8.0	7.07	7.12 ± 0.13	7.89
$He^{2+}/H^+(\times10^{-2})$	2.24 ± 0.11	4.40 ± 0.07	0.945	2.12	3.47 ± 0.01	2.08
$He/H(\times10^{-2})$	9.60 ± 0.47	10 ± 5	9	9.2	10.0 ± 1.3	10
$O^\circ/H^+(\times10^{-7})$	1.22 ± 0.30	–	0.211	–	–	–
$O^+/H^+(\times10^{-6})$	(6.7 ± 1.6)(†)	(2.23 ± 0.90) (††)	--	(5.1) (††)	(1.4 ± 0.1) (††)	3.33
$O^{2+}/H^+(\times10^{-4})$	2.11 ± 0.41	2.59 ± 0.21	2.34	3.78	2.36 ± 0.06	2.8
$O^{3+}/H^+(\times10^{-5})$	–	–	–	4.3	–	35.1
$O/H(\times10^{-4})$	(2.53 ± 0.48) (†)	4.44 ± 0.36	2.55	3.80	3.09 ± 0.09	3.3
ICF(O)	1.2 ± 0.3	1.70 ± 0.05	1.07	1	1.30 ± 0.01	1.17
$S^+/H^+(\times10^{-8})$	1.55 ± 0.25	–	0.602	1.80	0.93 ± 0.02	0.337
S^{2+}/H^+ $(\times10^{-7})$	6.00 ± 0.95	–	7.43	8.3	6.1 ± 0.2	6.62
$S^{3+}/H^+(\times10^{-6})$	–	–	–	1.94	–	–
$S/H(\times10^{-6})$	(1.40 ± 0.25) (†)	–	2.24	2.80	2.60 ± 0.11	2.4
ICF(S)	(2.3 ± 0.2) (†)	–	3.00	1	4.20 ± 0.11	3.52
$N^\circ/H^+(\times10^{-8})$	2.32 ± 0.95	–	–	–	–	–
$N^+/H^+(\times10^{-7})$	(3.00 ± 0.60)(†)	–	2.63	4.1	1.9 ± 0.1	3.2
$N^{2+}/H^+(\times10^{-5})$	–	–	–	5.7	–	2.2
$N^{3+}/H^+(\times10^{-6})$	–	–	–	43.9	–	6.77
$N^{4+}/H^+(\times10^{-5})$	–	–	–	3.6	–	2.35
$N/H(\times10^{-5})$	(1.50 ± 0.41) (†)	–	2.05	13.5	4.19 ± 0.39	3.4
ICF(N)	49 ± 14	–	80	1	220 ± 17.0	1.53

Notes. The pseudo-slit employed for our estimations is centered at the center of the PN with dimensions 36.8″× 42.6″. For the ionic abundances from previous studies, in the case where many emission lines were employed, and the adopted value was not available, the mean value of the individual ionic abundances was accounted in the table. (†)The resulted values after the correction for recombination contribution. (††)Only [O II] $\lambda\lambda$3726,3729 (blended) were available for the estimation of O^+/H^+. (†††)In the case of MH16, the values in the table are those that came from the pseudo-slit that covers the full region. Miller et al. (2016):MH16, Monteiro et al. (2013):MG13, Pottasch & Bernard-Salas (2008):PB08, Krabbe & Copetti (2006):KC06, Tsamis et al. (2003):TS03.

cover wavelengths below 4800 Å, skipping the detection of the O II recombination lines at ~4650 Å. Thus, we employed the Eq. (2) from Liu et al. (2000) to account for the recombination contribution.

As we only have [O III] collisionally excited lines in our spectrum, we adopted $O^{2+}/H^+ = 2.11\times10^{-4}$ and (as in the case of [N II] λ5755) T_e =12 700 K. With these values, the recombination contribution is estimated to be ~20% of the observed intensity relative to Hβ=100, which is in good agreement (within the errors) with previous studies (Tsamis et al. 2003). The corrected intensity is therefore I([O II] $\lambda\lambda$7320,7330)/ I(Hβ) = 0.85, which leads to $O^+/H^+ = 6.70 \times 10^{-6}$ and $O/H = 2.50 \times 10^{-4}$, instead of 8.18×10^{-6} and 2.60×10^{-4}, respectively. However, it is worth mentioning that although the total O abundance is little affected, the ionization degree of the nebula (given by the O^+/O^{2+} ratio) is strongly affected. On the other hand, if we adopt the O^{2+}/H^+ obtained from recombination lines by Tsamis et al. (2003), we obtained a recombination contribution that is even higher to the measured intensity of the line. This is a weird result as most of the emission of the [O II] $\lambda\lambda$7320,7330 lines arises from the LISs, where no recombination emission from heavy elements is seen (see Fig. 13). Gómez-Llanos et al. (2024) found a similar overestimation of recombination contribution using this formula in their analysis of MUSE data of NGC 6153. We therefore recommend adopting (whenever possible) both Liu et al. (2000) and García-Rojas et al. (2022) approaches to check consistency between them. We also refer the reader to the discussions by Liu et al. (2000); García-Rojas et al. (2022) and Gómez-Llanos et al. (2024) on this issue. Due to the lack of information on both the total flux and the spatial distribution of the O II recombination lines, we decided not to apply such corrections to the emission maps of [O II].

3.8.2. Comparison with previous studies

In general, several studies have examined the chemical composition of NGC 3242, using both IFU data (Monteiro et al. 2013, MG13) and slit spectroscopy (Miller et al. 2016; Pottasch & Bernard-Salas 2008; Krabbe & Copetti 2006; Tsamis et al. 2003, MH16, PB08, KC06, and TS03, respectively). MG13 and KC06 studied this PN using optical data, while MH16 used HST spectra ranging from ultraviolet (UV) to near-infrared (NIR), obtained during the HST Cycle 19 (Dufour et al. 2015). In the study of PB08, UV, optical, and NIR data were used as well, while TS03 scanned several PNe using a slit in the optical spectrum, supplementing the analysis with archival UV data from the International Ultraviolet Explorer (IUE). Table 4 presents the physical (T_e, n_e) and chemical properties of NGC 3242 from a pseudo-slit that covers the entire nebula (described in Sect. 3.8), as well as the results from previous studies. All the studies mentioned above used ICF schemes to compute elemental abundances; the sole exception is PB08, where the authors took advantage of a multiwavelength analysis and considered ICF = 1 for every element.

Regarding the physical parameters, T_e and n_e, the estimated values are in good agreement, within the errors, among all studies. There is also general agreement between the different studies for He/H and He^+/H^+. However, He^{2+}/H^+ in the present study agrees well with PB08 and TS03, but is nearly twice as high compared to the estimates from MG13 and KC06 and about half the value reported by MH16. In their study, MH16 examined the chemical homogeneity of NGC 3242 by splitting the main slit from the HST observations into nine smaller regions, determining the physicochemical properties of this PN in each specific region. Using the specific slit analysis module of SATELLITE, ten pseudo-slits were replicated as illustrated in Fig. 1 of MH16, to compare He/H and O/H in every region. For the total He abundance, our results agree well with MH16 within the errors. However, O/H values from MH16 are twice as high as our estimates.

Regarding the sulphur abundance, we estimated that it is $(1.40 \pm 0.40) \times 10^{-6}$ while all previous studies found S/H from 2.2×10^{-6} to 2.8×10^{-6}. A similar behavior was found for N/H, with estimates from the literature ranging from 2.05×10^{-5} to 13.5×10^{-5}, which are between 37% and 89% higher than our estimated value. We further discuss the significance of these discrepancies in Sect. 4.3.

3.9. Diagnostic diagrams

Diagnostic diagrams (hereafter, DDs) are designed to compare the relative line intensity ratios of certain emission lines commonly observed in PNe, supernova remnants (SNRs), and H II regions. Each of these types of objects is expected to occupy a distinct region on the DDs, mainly due to their different excitation mechanisms. These diagrams are widely used to identify the aforementioned nebulae (see, Frew & Parker 2010; Sabin et al. 2013; Kopsacheili et al. 2020). One of the most well-known DDs uses the ratio Hα/[N II] versus Hα/[S II] (Sabbadin et al. 1977; Riesgo & López 2006; Leonidaki et al. 2013). Another widely used DD relies on the [O III]/Hβ versus [S II]/Hα ratio, introduced by Baldwin et al. (1981), to distinguish H II regions, Seyfert galaxies, LINERS, and PNe. DDs were initially developed from long-slit spectroscopic data. However, spatially resolved DDs have been used for the identification of shock-excited regions or LISs in PNe (Barría & Kimeswenger 2018a,b), and DDs in conjunction with datacubes have also been used to identify SNRs (Monreal-Ibero et al. 2023; Kopsacheili et al. 2024). Additionally, DDs have been employed to investigate the ionization structure and excitation mechanisms of PNe (Akras et al. 2020b; Mari et al. 2023a).

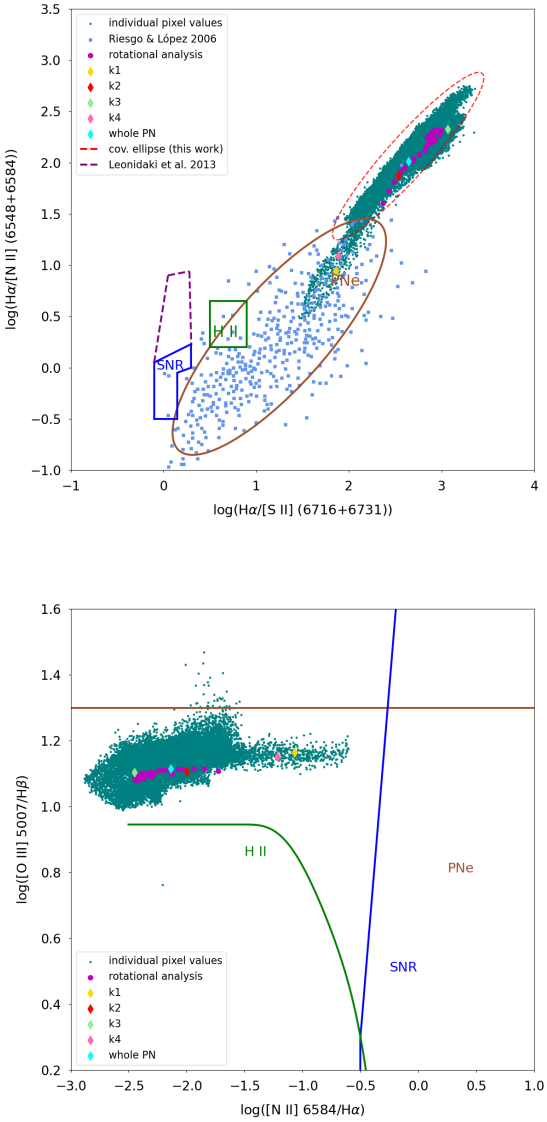

Fig. 14. Upper panel: log(Hα/[N II] (6548+6584)) versus log(Hα/[S II] (6716+6731)). Lower panel: log([O III] (4959+5007)/Hβ) versus log([N II] (6548+6584)/Hα). The brown, blue+purple and green regions define the positions of PNe, SNRs, and H II regions, respectively (Leonidaki et al. 2013; Riesgo & López 2006). The cyan dots are data points from the spaxel-by-spaxel analysis, the diamonds correspond to results from the specific slit analysis, and the pink dots indicate the findings from the rotational analysis. In the upper panel, the red dotted ellipse extends the PNe region to include the higher ionization PNe such as NGC 3242.

To perform a direct comparison between 1D and 2D analysis, we ran the following SATELLITE modules: 2D analysis, specific slit analysis and rotational analysis, indicated as cyan dots, diamonds (colored on the basis of the pseudo-slit's position) and pink dots on the DDs shown in Fig. 14, respectively. For the specific slit analysis, four pseudo-slits were placed at the positions of the four knots (see, Fig. 3) and another one covering the entire nebula was also used (pseudo-slit dimensions 36.8″ × 42.6″). The rotational analysis was performed from PA 0° to 360°, with

10° steps. Since DDs were initially developed for 1D spectroscopic data, the results of the 2D analysis can only provide a glimpse into the distribution of each spaxel's value on these diagrams. This approach was previously used by Akras et al. (2020b), who analyzed the emission line ratios of each individual spaxel of Abell 14 on the DDs.

Overall, the cyan dots and the results from the slit analysis follow the same trend on these diagrams, indicating that the spaxel-by-spaxel representation on the DDs is well-defined. In the case of Hα/[N II] versus Hα/[S II] diagram (Fig. 14, top panel) most of the cyan points lie outside the ellipse where PNe are expected to be, occupying a wide range of values from 0.5 to 3 for log(Hα/[N II] (6548+6584)) and from 1 to 3.5 for log(Hα/[S II] (6716+6731)). The brown ellipse marked on Fig. 14 is a density ellipse with 85% probability (2 σ), which was derived from a sample of 613 PNe (light blue squares in Fig. 14) (Riesgo & López 2006). To extend the region of PNe on this DD and account for high-ionization nebulae, such as NGC 3242, we formulated covariance ellipse with 99% probability (3 σ) based on the data points of NGC 3242 (red dotted ellipse in Fig. 14). It is worth noting that many spaxels from NGC 7009 have also been found outside the brown ellipse (see Fig. 11 in Akras et al. 2022b), as well as spaxels from 1D photoionization models with high log(U) parameter, namely, highly ionized nebulae (see Fig. 5 in Akras et al. 2020b). However, for a more general representation, a larger sample of high-ionization nebulae is needed and should be considered. [2]

A similar behavior is observed in the log([O III] (4959+5007)/Hβ) versus log([N II] (6548+6584)/Hα) DD. Although all points are within the PNe region, the values for the log([N II] (6548+6584)/Hα) ratio indicate that the intensity of Hα is significantly higher than that of [N II]. These results reinforce the picture of a highly ionized PN (Pottasch et al. 1984), leading to higher values of the emission line ratios involved in the DDs. However, it should be noted that the values of the [N II] (6548+6584)/Hα ratio are also affected by the metallicity of the nebula. The results from the specific slit analysis (colored diamonds) follow the same trend as the 2D and rotational representations. Only the pseudo-slits that are placed at the LISs (k1 and k4), exhibit higher log([N II] (6548+6584)/Hα), since the ionization degree there is lower by definition.

Generally, caution is needed when these diagrams are used with spaxel values from IFU data due to possible degeneracies that may lead to misinterpretation of the results (see a paradigmatic example presented by Morisset 2018). The emission line ratios for the pseudo-slit that covers the whole PN (light-blue diamond) serve as indicators of the scattering of the spaxel-by-spaxel values. Specifically, log([O III]λ5007/Hβ) is 1.14, with spaxel values ranging from −0.04 to +0.39 (±0.02 for high flux-to-error (F/E) spaxels and ±0.04 for low F/E spaxels) [3]. The log(Hα/[S II](6716+6731)) ratio has a central value of 2.64, with spaxel values spanning from −1.16 to +0.76 (±0.09 for high F/E and ±0.10 for low F/E spaxels). For log(Hα/[N II](6584+6548)), the ratio is 2.01, with deviations ranging from −2.20 to +0.69 (±0.04 for high F/E and ±0.05 for low F/E). Lastly, log([N II](6584)/Hα) yields −2.14, with deviations ranging from −0.72 to +1.54 (±0.01 for high F/E and ±0.02 for low F/E spaxels).

[2] log(U) is the logarithmic ratio of the ionizing photon density to hydrogen density.

[3] High F/E spaxels are considered those with Hβ flux-to-error ratio above 70 and the rest of them are the low F/E spaxels. The first ones lye in the inner nebular regions and the others at the outer shell.

4. Discussion

4.1. Nebular shell

MUSE offers the capability to examine in detail the spatial distribution of various emission lines. The deeper investigation of MUSE datacubes led to the detection of new structures in the nebular shell. These regions are mainly seen in the light of [S III] and [N II]. According to Ramos-Larios & Phillips (2009), the fragmented halo of NGC 3242, as revealed from Spitzer, is interacting with the ISM which could possibly cause the diffusion of ISM material into the nebular shells. Additionally, hydrodynamical instabilities in the inner nebular structures could yield to enhanced emission at the leading edges of the nebular shell. On the contrary, the [Fe III] emission that has been detected in these structures, may indicate shock interactions (Bouvis et al., in prep.). However, the ratios of [S II]/Hα and [N II]/Hα reveal no trend for shock activity at these regions. So, further investigation is needed to understand their origin.

Two arc-like structures were also detected in the shell at the edges of the two LISs (see Fig. 3). These could be related to the new structures found perpendicular to the LISs, since they share the same physico-chemical properties. However, the position of the arcs could also indicate an association with the LISs. Thus, we have no evidence for this assumption at present, so we leave this aspect to a future study.

4.2. Physical parameters and excitation mechanisms

In the present study, T_e was calculated from both CELs and ORLs. In every case, there is a trend toward higher temperatures in the inner nebular structures. We see that T_e ([S III]) and T_e ([N II]) values are systematically higher than those of T_e (PJ) and T_e (He I), with the latter being the lowest of all the estimated T_e values. The mean values for each T_e from the 2D temperature maps, with 1σ confidence intervals, are T_e ([S III]) = (12 500 ± 1700) K, T_e ([N II]) = (11 700 ± 1500) K, T_e (PJ) = (8900 ± 3700) K, and T_e (He I) = (7800 ± 1000) K (see Table 3). The fact that T_e is systematically higher when it is derived from CELs instead of ORL diagnostics, such as H I Balmer and/or Paschen discontinuities, is a well known issue. This discrepancy has been attributed whether to the presence of temperature inhomogeneities in the gas (Peimbert 1967) or to the effect of chemically inhomogeneities (Liu et al. 2000; Zhang et al. 2005a). On the other hand, the behavior between T_e (He I) and T_e (PJ) is consistent with what was found for a sample of 48 PNe by Zhang et al. (2005a) (T_e (He I) < T_e (H I)). These authors considered this behavior to be consistent with the expectations of a chemically inhomogeneous nebula model. However, in a recent paper, Méndez-Delgado et al. (2024) have found that a combination of temperature inhomogeneities and deviations from "case-B" recombination scenario can explain the observed discrepancies between T_e (He I) and other temperature diagnostics. It is not trivial to assess the contribution of each scenario to this discrepancy. Méndez-Delgado et al. (2024) propose a toy model with a mixed "case A" + "case B" scenario to check whether deviations from "case B" could account for the temperature discrepancies. This can be done by using the fact that "case A" and "case B" He I line emissivities originating from n^1P levels differ substantially. Unfortunately, the only transition originating from a n^1P level in the wavelength range covered by MUSE is He I λ5016, whose emission line map in the long-exposure datacube could not be extracted owing to the proximity of [O III] λ5007 line, which is strongly saturated; alternatively, we tried to extract it in

the 10s exposure datacube, but the obtained map was too noisy to draw any significant conclusion.

Regarding the electron density, a trend toward higher values is observed at the nebular rim, while no significant difference is observed between n_e ([S II]) = (2200 ± 1500) cm^{-3} and n_e ([Cl III]) = (1600 ± 1000) cm^{-3} (see Table 3).

4.3. Nebular chemical composition

The chemical properties of NGC 3242 estimated from this study are generally in good agreement with previous results from the literatue. However, there is a trend toward higher values for O/H with the biggest difference arising from MH16. The value of MH16 for the entire region (included in Table 4) is closer to the value reported by PB08, but still higher. It is worth mentioning though that MH16 used the recipe of Kwitter & Henry (2001) for the ICF(O). Based on this approach, ICF is a linear representation of the (He^++ He^{2+})/ He^+ ratio, in contrast to the ICF(O) that is employed in this work, which depends on a power of 2/3 of the same ratio (see Eq. (A9) in Kingsburgh & Barlow 1994).

Also, the discrepancy in S abundance among our study with the previous ones, is significant. We suggest that the difference arises from the lower ionization degree (O^+/O) obtained from our data compared to the literature values, which translates into a lower ICF. As mentioned above, PB08 took advantage of a multi-wavelength analysis and thus do not adopt any ICF to compute the total S abundance, which is ∼50% higher than the one computed in this work.

Similarly, N/H is notably higher, than our estimation (Table 4). However, the computation of total N abundances from optical spectra in high-excitation PNe is controversial, because of the extremely large and uncertain corrections that should be adopted. PB08 computed the N abundance without adopting an ICF, by combining N^+ ionic abundances from the optical and N^{2+}, N^{3+}, and N^{4+} from ultraviolet (UV) and far-infrared observations (see values in Table 4). With these data they estimated a log (N/O) ∼ −0.44, which is much higher than the N/O ratios estimated from other literature sources (including TS03 which also used UV and far-infrared observations to compute N^{2+}, and N^{3+}), that imply log (N/O) ratios between −0.86 and −1.14. However, it is worth mentioning that TS03 and PB08 obtained very different N^{2+}, and N^{3+} abundances from different sets of UV and far-infrared data and that several of these values were reported by these authors as highly uncertain. Moreover, N^{2+} abundance from the far-infrared N III] 57.3μm line is very density-dependent, finding differences up to a factor of 2, depending on the adopted n_e (see discussion in Sect. 5.2 from TS03).

4.4. The low-ionization structures

4.4.1. Emission of atomic carbon from the LISs

Overall, LISs are small scale structures with strong emission in low ionization species, compared to the surrounding nebula. Commonly, [N II], [S II], and [O I] are identified in the LISs of PNe. In this study, the investigation of MUSE data led to the detection of the [C I] λ8727 emission line, too. The same line of neutral C has also been detected in the LISs of NGC 7009 (Akras et al. 2024). In addition, atomic O is also mainly emitted from the pair of LISs, (see Fig. 6 right panels). This co-existence has been previously noticed in the knotty structures of NGC 6778, and M 1-42 (García-Rojas et al. 2022). The co-spatial distribution of atomic C and atomic O emissions, may imply the dissociation of CO due to the intense UV radiation from the CS, but further investigation is needed (Gonçalves et al. in preparation). CO has been previously identified in the cometary knots of Helix nebula (Huggins et al. 1992; Andriantsaralaza et al. 2020), while Moraga Baez et al. (2023), using ALMA observations, detected CO in the clumpy structures of several PNe.

Molecular hydrogen (H_2) emission has also been found to originate in LISs (Akras et al. 2017; Akras et al. 2020a; Fang et al. 2015, 2018). In the case of NGC 7009, the ionization stratification was found to be equivalent to a mini-PDR surrounding a molecular/H_2 core (Akras et al. 2020a; Akras et al. 2024). More specifically, the high-ionization lines peak closer to the CS than the low ionization ones and then the atomic lines follow the sequence. Furthermore, in the case of NGC 7009, molecular lines of H_2 were found. In the present study on NGC 3242, the radial analysis indeed revealed that the high-ionization lines (Hα, Hβ, [O III], He II, and [S III]) peak at the nebular rim while the low ionization ([N II] and [S II]) and neutral ([O I] and [C I]) lines peak at the LISs. Generally, there is no significant offset between the peaks of the low ionization lines. Interestingly, though, in the case of the high-to-moderate ionization lines, a different stratification is observed among the two PA. We suggest, that this divergence more likely occurs due to the orientation of the nebula and the shock emission due to the interaction of the inner jet with the rim (see Section 3.3). The above may complicate the surface brightness profiles.

4.4.2. Search for H_2 in Spitzer data

In the LISs of NGC 3242, n_e was found lower compared to the main nebular structures, while theoretical models predict the exact opposite. This problem could be ruled out if molecular gas exists in LISs of NGC 3242, such as the low-ionization features of other PNe (Speck et al. 2003; Kwok et al. 2008; Matsuura et al. 2009; Fang et al. 2015; Akras et al. 2017; Fang et al. 2018; Akras et al. 2020a; Wesson et al. 2023); however, until now, there has been no direct evidence for this. In an attempt to further investigate the assumption of H_2 presence at the LISs, archival data from Spitzer Space Telescope (SST) for NGC 3242 were utilized to search for H_2 in Infrared Array Camera (IRAC) bands. IRAC is a four-channel camera that provides simultaneous 5.2′ × 5.2′ images at 3.6, 4.5, 5.8, and 8.0 μm. The filters had bandwidths $\Delta\lambda$ = 0.75 μm, $\Delta\lambda$ = 1.902 μm, $\Delta\lambda$ = 1.425 μm, and $\Delta\lambda$ = 2.905 μm. At the position of the LISs in the planetary nebula NGC 7009, the ratios of the IRAC filters with the 4.5 μm were seen to be decreasing (Phillips et al. 2010). It was suggested that this decrease is associated with an increase in emission from the 4.5 μm band. Akras et al. (2020a) proposed that the primary emission in this band is likely H_2. However, in the case of NGC 3242, the LISs were not detectable in any of IRAC bands. This lack of observation suggests that the emission from H_2 is either faint or absent.

A correlation between the intensities of [O I] λ6300 line and the l–0 S(1) ro-vibrational line of H_2 was introduced by Reay et al. (1988). The results about a sample of ten PNe is presented in their Fig. 2. Based on that plot, we can have an indication about the flux of H_2 given the flux of [O I]. In the case of NGC 3242, the flux of [O I] λ6300 line integrated at the LISs is on the order of 10^{-14} erg cm^{-2} s^{-1}, which implies a flux of H_2 around 10^{-16} erg cm^{-2} s^{-1}. This flux is translated in a flux density of 10^{-32} erg cm^{-2} s^{-1} Hz^{-1}, given the bandwidth of the filter and the exposure time of the observations. In the same exposure time, the sensitivity of IRAC in the 4.5 μm band, reaches a sensitivity of ∼10^{-29} erg cm^{-2} s^{-1} Hz^{-1}. Thus, if there

is indeed H_2 emission, it would be really difficult to be detected from broadband filters, such as the ones provided from IRAC.

4.4.3. [Fe II] and [Fe III] emission from the LISs

In addition to the detection of the [Fe II] λ8617 line from the LISs, the [Fe III] λ5270 line was also detected, showing the presence of a jet-like structure that connects the central star and the LISs. In general, iron is considered as shock indicator; thus, in the case of NGC 3242, Fe is probably released and ionized from shocks as well. However, we plan to further investigate the origin of iron emission in a follow-up study (Bouvis et al., in prep.). Moreover, the formation of a jet could indicate the existence of a binary progenitor, consisting of a companion star rotating around an AGB star (Soker & Livio 1994). The scenario of a multiple star system, at the center of NGC 3242, has been previously reported from Soker et al. (1992). It is interesting though that the jet is asymmetric, with the northwest part being more extended. The X-ray emission, found in NGC 3242, also appears stronger in the same direction (Ruiz et al. 2011). However, from Fig. 5, it is clear that k1 is red-shifted while k4 is blue-shifted, so it is possible that the orientation of the PN is responsible for both the asymmetry of the jet and the enhanced X-ray emission at the northwest nebular regions.

The interaction of the jet with the rim may be responsible for the formation of the blobs (b1 and b2) and possibly the knots. In particular, the k2 and k3 structures are characterized by higher [O III]/[O I] and [S III]/[S II] ratios compared to the host nebula. Thus, the enhanced emission of [O III] and [S III] at the rim, along with the formation of knotty structures along the direction of the LISs, could also be an aftermath of the jet-rim interaction. Nevertheless, there is no discrepancy in T_e among the different regions (Table A.2). In conclusion, we argue that there is a correlation between the knots and the newly discovered jet-like structure, which may also imply their shock excitation. Although this seems to contradict the lower n_e value found for k1 and k4, the higher densities expected in shock environments could be explained by a molecular component, as n_e reflects only the ionized gas fraction. We plan to further examine the dominant excitation mechanism of k1 and k4 in an upcoming paper (Bouvis et al., in prep.).

5. Conclusions

In this study, we investigate the physico-chemical properties of NGC 3242 using MUSE IFU data in conjunction with the SATELLITE code. A detailed examination of the emission line maps allowed us to identify new structures embedded in the nebular shell, oriented perpendicular to the pair of LISs. These structures may represent the aftermath of instabilities in the inner nebular structures. However, we cannot rule out the possibility of shock interactions. Two arc-like structures were also identified at the edges of the LISs. We suggest that these are probably linked to the enhanced emission of the nebular shell, but they could also be associated with the pair of LISs. The extinction coefficient (c(Hβ)), calculated from H I Balmer lines, shows no significant variation throughout the nebula, with a mean value of 0.14. T_e([N II]) and T_e([S III]) are approximately 11 8700 K and 12 500 K, respectively, while n_e ([S II]) and n_e ([Cl III]) values are around 2200 and 1600 cm^{-3}, respectively. Regarding T_e values from ORLs, we found that T_e (PJ) is 8900 and T_e(He I) is 7800 K, estimated in an ellipse that covers the inner nebular structures to avoid the contamination from the T_e outside the rim. Unfortunately, the data were not deep enough to test whether the discrepancy between T_e (PJ) and T_e (He I) could be the aftermath of deviations from the "case B."

The diagnostic diagrams provided by SATELLITE, revealed that NGC 3242 is a highly ionized nebula and its dominant excitation mechanism is photoionization. In terms of the chemical composition of this PN, there is no significant variation throughout the nebular structures. Our results are consistent with those of previous studies, except for the elemental abundances of O, S, and N. For O/H, the biggest difference arises in the case of MH16, where a different ICF(O) recipe has been used. Regarding, N/H and S/H, since NGC 3242 is a highly ionized PN, the contribution from triply ionized N and S lines (not available in optical data) is crucial.

The [C I] λ8727 atomic line was identified in MUSE data, originating mainly from the LISs. The co-existence of [C I] and [O I] at the LISs may suggest the dissociation of CO molecules; however, until now, there is no direct confirmation of this hypothesis. Additionally, through the radial analysis module, we found that the atomic lines of [C I] and [O I] as well as other low-ionization lines peak closer to the LISs compared to moderate-to-high-ionization lines. Thus, LISs may consist of a molecular core surrounded by highly ionized gas, which is further enclosed by a partially ionized gas. In the present study, we have not been able to detect H_2 through Spitzer IRAC data, but further investigation is needed to confirm the existence or absence of H_2 at the LISs of NGC 3242.

Moreover, iron emission was detected in the spectrum of NGC 3242. More precisely, [Fe II] λ8617 was found to emanate from the LISs and [Fe III] λ5270 was detected in a jet-like structure that extends from the center of the nebula to the LISs. This finding may suggest that the knots and the jet-like structure are correlated. We also argue that both [Fe II] and [Fe III] are probably shock-originated, while the presence of the jet could also indicate the existence of a binary progenitor.

Acknowledgements. The research project is implemented in the framework of H.F.R.I. call "Basic research financing (Horizontal support of all Sciences)" under the National Recovery and Resilience Plan "Greece 2.0" funded by the European Union–NextGenerationEU (H.F.R.I. Project Number: 15665). JGR acknowledges financial support from the Agencia Estatal de Investigación of the Ministerio de Ciencia e Innovación (AEI- MCINN) under Severo Ochoa centers of Excellence Programme 2020–2023 (CEX2019-000920-S), and from grant "Planetary nebulae as the key to understanding binary stellar evolution" with reference number PID-2022-136653NA-I00 (DOI:10.13039/501100011033) funded by the Ministerio de Ciencia, Innovación y Universidades (MCIU/AEI) and by ERDF "A way of making Europe" of the European Union. The authors would like to acknowledge Dr. Henri Boffin for the reduction of the MUSE data. The following software packages in Python were used: Matplotlib (Hunter 2007), NumPy (van der Walt et al. 2011), SciPy (Virtanen et al. 2020) and AstroPy Python (Astropy Collaboration 2013, 2018).

References

Akras, S., & Gonçalves, D. R. 2016, MNRAS, 455, 930
Akras, S., Gonçalves, D. R., & Ramos-Larios, G. 2017, MNRAS, 465, 1289
Akras, S., Gonçalves, D. R., Ramos-Larios, G., & Aleman, I. 2020a, MNRAS, 493, 3800
Akras, S., Monteiro, H., Aleman, I., et al. 2020b, MNRAS, 493, 2238
Akras, S., Monteiro, H., Walsh, J. R., et al. 2022a, Galaxies, 10, 27
Akras, S., Monteiro, H., Walsh, J. R., et al. 2022b, MNRAS, 512, 2202
Akras, S., Monteiro, H., Walsh, J. R., et al. 2024, A&A, 689, A14
Aleman, I., Zijlstra, A. A., Matsuura, M., Gruenwald, R., & Kimura, R. K. 2011, MNRAS, 416, 790
Andriantsaralaza, M., Zijlstra, A., & Avison, A. 2020, MNRAS, 491, 758
Astropy Collaboration (Robitaille, T. P., et al.) 2013, A&A, 558, A33
Astropy Collaboration (Price-Whelan, A. M., et al.) 2018, AJ, 156, 123
Bailer-Jones, C. A. L., Rybizki, J., Fouesneau, M., Demleitner, M., & Andrae, R. 2021, AJ, 161, 147

Baldwin, J. A., Phillips, M. M., & Terlevich, R. 1981, PASP, 93, 5
Balick, B. 1987, AJ, 94, 671
Balick, B., & Frank, A. 2002, ARA&A, 40, 439
Balick, B., Alexander, J., Hajian, A. R., et al. 1998, AJ, 116, 360
Balick, B., Frank, A., & Liu, B. 2020, ApJ, 889, 13
Balick, B., Rugers, M., Terzian, Y., & Chengalur, J. N. 1993, ApJ, 411, 778
Barría, D., & Kimeswenger, S. 2018a, Galaxies, 6
Barría, D., & Kimeswenger, S. 2018b, MNRAS, 480, 1626
Benjamin, R. A., Skillman, E. D., & Smits, D. P. 1999, ApJ, 514, 307
Bhatia, A. K., & Kastner, S. O. 1995, ApJS, 96, 325
Butler, K., & Zeippen, C. J. 1989, A&A, 208, 337
Cardelli, J. A., Clayton, G. C., & Mathis, J. S. 1989, ApJ, 345, 245
Corradi, R. L. M., Manso, R., Mampaso, A., & Schwarz, H. E. 1996, A&A, 313, 913
Corradi, R. L. M., Schönberner, D., Steffen, M., & Perinotto, M. 2003, MNRAS, 340, 417
Delgado-Inglada, G., Morisset, C., & Stasińska, G. 2014, MNRAS, 440, 536
Delgado-Inglada, G., Mesa-Delgado, A., García-Rojas, J., Rodríguez, M., & Esteban, C. 2016, MNRAS, 456, 3855
Dopita, M. A., Mason, D. J., & Robb, W. D. 1976, ApJ, 207, 102
Dufour, R. J., Kwitter, K. B., Shaw, R. A., et al. 2015, ApJ, 803, 23
Fang, X., Storey, P. J., & Liu, X. W. 2011, A&A, 530, A18
Fang, X., Guerrero, M. A., Miranda, L. F., et al. 2015, MNRAS, 452, 2445
Fang, X., Zhang, Y., Kwok, S., et al. 2018, ApJ, 859, 92
Frew, D. J., & Parker, Q. A. 2010, PASA, 27, 129
Froese Fischer, C., & Tachiev, G. 2004, At. Data Nucl. Data Tables, 87, 1
Froese Fischer, C., Tachiev, G., & Irimia, A. 2006, At. Data Nucl. Data Tables, 92, 607
García-Rojas, J., Morisset, C., Jones, D., et al. 2022, MNRAS, 510, 5444
Gómez-Llanos, V., García-Rojas, J., Morisset, C., et al. 2024, A&A, 689, A228
Gonçalves, D. R., Corradi, R. L. M., & Mampaso, A. 2001, ApJ, 547, 302
Gonçalves, D. R., Corradi, R. L. M., Mampaso, A., & Perinotto, M. 2003, ApJ, 597, 975
Gonçalves, D. R., Mampaso, A., Corradi, R. L. M., & Quireza, C. 2009, MNRAS, 398, 2166
Gómez-Muñoz, M. A., Blanco Cárdenas, M. W., Vázquez, R., et al. 2015, MNRAS, 453, 4175
Hajian, A. R., Balick, B., Terzian, Y., & Perinotto, M. 1997, ApJ, 487, 304
Henney, W. J., & Valerdi, M. 2024, MNRAS, 529, 1723
Howarth, I. D., & Wilson, B. 1983, MNRAS, 204, 1091
Huggins, P. J., Bachiller, R., Cox, P., & Forveille, T. 1992, ApJ, 401, L43
Hunter, J. D. 2007, CiSE, 9, 90
Icke, V. 1988, A&A, 202, 177
Kaufman, V., & Sugar, J. 1986, JPCRD, 15, 341
Kingsburgh, R. L., & Barlow, M. J. 1994, MNRAS, 271, 257
Kisielius, R., Storey, P. J., Ferland, G. J., & Keenan, F. P. 2009, MNRAS, 397, 903
Kopsacheili, M., Zezas, A., & Leonidaki, I. 2020, MNRAS, 491, 889
Kopsacheili, M., Jiménez-Palau, C., Galbany, L., Boumis, P., & González-Díaz, R. 2024, MNRAS, 530, 1078
Krabbe, A. C., & Copetti, M. V. F. 2005, A&A, 443, 981
Krabbe, A. C., & Copetti, M. V. F. 2006, A&A, 450, 159
Kwitter, K. B., & Henry, R. B. C. 2001, ApJ, 562, 804
Kwok, S., Chong, S.-N., Koning, N., Hua, T., & Yan, C.-H. 2008, ApJ, 689, 219
Leonidaki, I., Boumis, P., & Zezas, A. 2013, MNRAS, 429, 189
Liu, X. W., Storey, P. J., Barlow, M. J., et al. 2000, MNRAS, 312, 585
Luridiana, V., Morisset, C., & Shaw, R. A. 2015, A&A, 573, A42
Mari, M. B., Akras, S., & Gonçalves, D. R. 2023a, MNRAS, 525, 1998
Mari, M. B., Gonçalves, D. R., & Akras, S. 2023b, MNRAS, 518, 3908
Matsuura, M., Speck, A. K., McHunu, B. M., et al. 2009, ApJ, 700, 1067
Meaburn, J., López, J. A., & Noriega-Crespo, A. 2000, ApJS, 128, 321
Méndez-Delgado, J. E., Esteban, C., García-Rojas, J., et al. 2021, MNRAS, 502, 1703
Méndez-Delgado, J. E., Skillman, E. D., Aver, E., et al. 2024, arXiv e-prints [arXiv:2410.17381]
Miller, T. R., Henry, R. B. C., Balick, B., et al. 2016, ApJ, 830, 9
Monreal-Ibero, A., Roth, M. M., Schönberner, D., Steffen, M., & Böhm, P. 2005, ApJ, 628, L139
Monreal-Ibero, A., Weilbacher, P. M., Micheva, G., Kollatschny, W., & Maseda, M. 2023, A&A, 674, A210
Monteiro, H., Gonçalves, D. R., Leal-Ferreira, M. L., & Corradi, R. L. M. 2013, A&A, 560, A102
Moraga Baez, P., Kastner, J. H., Bublitz, J., et al. 2023, in AAS Meeting Abstracts, 241, 468.02
Morisset, C. 2018, in Walking the Line 2018, 2
Morisset, C., Luridiana, V., García-Rojas, J., et al. 2020, Atoms, 8, 66
Munoz Burgos, J. M., Loch, S. D., Ballance, C. P., & Boivin, R. F. 2009, A&A, 500, 1253
Osterbrock, D. E. 1989, Astrophysics of Gaseous Nebulae and Active Galactic Nuclei
Peimbert, M. 1967, ApJ, 150, 825
Pequignot, D., & Aldrovandi, S. M. V. 1976, A&A, 50, 141
Pequignot, D., Petitjean, P., & Boisson, C. 1991, A&A, 251, 680
Perinotto, M. 2000, Ap&SS, 274, 205
Phillips, J. P., Ramos-Larios, G., Schröder, K.-P., & Contreras, J. L. V. 2009, MNRAS, 399, 1126
Phillips, J. P., Cuesta, L. C., & Ramos-Larios, G. 2010, MNRAS, 409, 881
Porter, R. L., Ferland, G. J., Storey, P. J., & Detisch, M. J. 2012, MNRAS, 425, L28
Porter, R. L., Ferland, G. J., Storey, P. J., & Detisch, M. J. 2013, MNRAS, 433, L89
Pottasch, S. R., & Bernard-Salas, J. 2008, A&A, 490, 715
Pottasch, S. R., Baud, B., Beintema, D., et al. 1984, A&A, 138, 10
Raga, A. C., Riera, A., Mellema, G., Esquivel, A., & Velázquez, P. F. 2008, A&A, 489, 1141
Ramos-Larios, G., & Phillips, J. P. 2009, MNRAS, 400, 575
Ramos-Larios, G., Guerrero, M. A., Toalá, J. A., Akras, S., & Fang, X. 2023, MNRAS, 527, 10123
Reay, N. K., Walton, N. A., & Atherton, P. D. 1988, MNRAS, 232, 615
Reiter, M., McLeod, A. F., Klaassen, P. D., et al. 2019, MNRAS, 490, 2056
Riesgo, H., & López, J. A. 2006, Rev. Mexicana Astron. Astrofis., 42, 47
Ruiz, N., Guerrero, M. A., Chu, Y.-H., & Gruendl, R. A. 2011, AJ, 142, 91
Rynkun, P., Gaigalas, G., & Jönsson, P. 2019, A&A, 623, A155
Sabbadin, F., Minello, S., & Bianchini, A. 1977, A&A, 60, 147
Sabin, L., Parker, Q. A., Contreras, M. E., et al. 2013, MNRAS, 431, 279
Seaton, M. J. 1979, MNRAS, 187, 73
Soker, N., & Livio, M. 1994, ApJ, 421, 219
Soker, N., Zucker, D. B., & Balick, B. 1992, AJ, 104, 2151
Speck, A. K., Meixner, M., Knezek, P., & Jacoby, G. H. 2003, in Planetary Nebulae: Their Evolution and Role in the Universe, 209, eds. S. Kwok, M. Dopita, & R. Sutherland, 271
Steffen, W., López, J. A., & Lim, A. 2001, ApJ, 556, 823
Storey, P. J., & Hummer, D. G. 1995, MNRAS, 272, 41
Storey, P. J., & Zeippen, C. J. 2000, MNRAS, 312, 813
Storey, P. J., Sochi, T., & Badnell, N. R. 2014, MNRAS, 441, 3028
Tayal, S. S. 2011, ApJS, 195, 12
Tayal, S. S., & Gupta, G. P. 1999, ApJ, 526, 544
Tayal, S. S., & Zatsarinny, O. 2010, ApJS, 188, 32
Temim, T., Laming, J. M., Kavanagh, P. J., et al. 2024, ApJ, 968, L18
Tsamis, Y. G., Barlow, M. J., Liu, X. W., Danziger, I. J., & Storey, P. J. 2003, MNRAS, 345, 186
van der Walt, S., Colbert, S. C., & Varoquaux, G. 2011, CiSE, 13, 22
Virtanen, P., Gommers, R., Oliphant, T. E., et al. 2020, Nat Methods 17, 261
Wesson, R., Matsuura, M., Zijlstra, A. A., et al. 2023, MNRAS, 528, 3392
Wiese, W., Fuhr, J., & Deters, T. 1996, Atomic Transition Probabilities for Carbon, Nitrogen and Oxygen
Zeippen, C. J. 1982, MNRAS, 198, 111
Zhang, Y., Liu, X. W., Liu, Y., & Rubin, R. H. 2005a, MNRAS, 358, 457
Zhang, Y., Rubin, R. H., & Liu, X. W. 2005b, in Rev. Mexicana Astron. Astrofis., 23, eds. S. Torres-Peimbert, & G. MacAlpine, 15

Appendix A: Supplementary tables

Table A.1: Observed and de-reddened line fluxes relative to Hβ=100.

Line (Å)	F(λ)	I(λ)
Hβ	100	100
[O III] 4959	435.0±8.7	432.0±8.7
[O III] 5007	1 314±26.4	1 299.0±26.5
[N I] 5200	0.016±0.002	0.016±0.002
He II 5412	2.14±0.11	2.05±0.1
[Cl III] 5517	0.032±0.03	0.31±0.03
[Cl III] 5538	0.30±0.03	0.28±0.03
[N II] 5755†	0.052±0.007	0.064±0.007
	0.032±0.03	0.049±0.005
He I 5876	11.97±0.63	12.0±0.6
[O I] 6300	0.105±0.011	0.096±0.010
[S III] 6312	0.76±0.08	0.70±0.08
[O I] 6363	0.041±0.001	0.04±0.01
[N II] 6548	0.76±0.04	0.70±0.04
Hα	319.0± 6.4	287.0±6.4
[N II] 6584	2.33±0.12	2.10±0.12
He I 6678	3.30±0.17	3.0±0.21
[S II] 6716	0.31±0.02	0.27±0.02
[S II] 6731	0.42±0.02	0.37±0.02
[Ar III] 7136	8.77±0.46	7.7±0.5
[O II] 7320†	0.63±0.07	0.55±0.06
	0.54±0.06	0.46±0.07
[O II] 7330†	0.56±0.06	0.50±0.06
	0.45±0.05	0.38±0.07
[C I] 8727	0.008±0.0001	0.0070±0.0001
[S III] 9069	7.6±0.4	6.3±0.5
F(Hβ)×10^{-14}	140.0±1.4	–
c(Hβ)	0.14	

Notes. The fluxes are integrated for a pseudo-slit that covers the whole PN (36.8″× 42.6 ″ and centered at the center of the PN). $^{(a)}$ For [N II] λ5755, the flux was estimated from the raw map $^{(b)}$ F(Hβ) is the reddened Hβ flux in unit erg cm^{-2} s^{-1}. $^{(\dagger)}$ The second row represents the values after correction for recombination contribution.

Table A.2: Physical parameters and emission line ratios, resulting from the specific slit analysis for the new structures (2nd column), the four knots (columns 3 to 6), and the surrounding environment of the new structures (final column).

	new structures	k1	k2	k3	k4	surrounding gas
			T_e(K)/n_e (cm^{-3})			
T_e ([S III])	11 600±660	11 700±660	12 100±760	14 900±1 100	11 700±700	11 900±790
T_e ([N II])	12 000±770	11 300±500	10 700±600	11 400±700	11 400±600	11 700±840
n_e ([Cl III])	900±500	1 200±870	3 100±1 300	2 300±1 100	1 400±800	900±300
n_e ([S II])	1 500±300	1 800±500	4 500±1 000	3 400±1 000	2 200±500	1 500±300
			Emission line ratios			
log ([S III]/[S II])	1.06±0.04	0.37±0.04	1.01±0.03	1.25±0.04	0.58±0.04	1.16±0.04
log ([O III]/[O I])	4.18±0.04	2.60±0.04	4.80±0.03	4.74±0.04	2.97±0.04	4.22±0.04
log ([N II]/Hα)	−2.04±0.03	−1.00±0.02	−1.90±0.02	−2.30±0.02	−1.20±0.02	−2.30±0.03
log ([S II]/Hα)	−2.54±0.03	−1.86 ±0.02	−2.54±0.02	−3.70±0.03	−2.10±0.02	−2.80±0.03
log ([N II]/[O III])	−2.85±0.02	−1.88±0.02	−2.69±0.02	−3.05±0.02	−1.85±0.02	−3.10±0.02

Notes. Where [S III], [S II], [O III], [O I] and [N II] stand for [S III] λ(6312+9069), [S II] λ(6716+6731), [O III] λ(4959+5007), [O I] λ(6300+6363) and [N II] λ(6548+6583), respectively.

Appendix B: 2D abundance maps

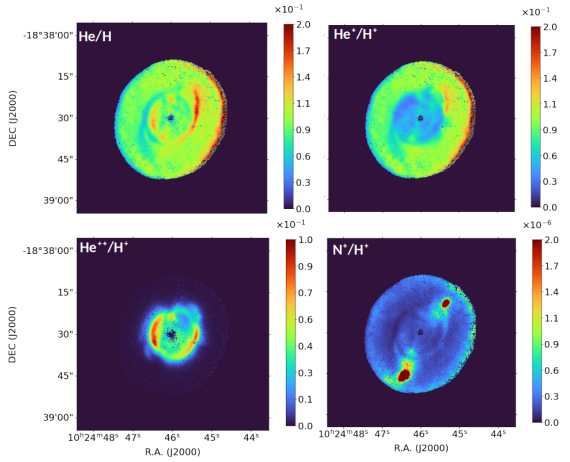

Fig. B.1: Ionic and elemental abundance maps. From left to right and from top to bottom: He/H, He^{+}/H^{+}, He^{2+}/H^{+}, and N^{+}/H^{+}.

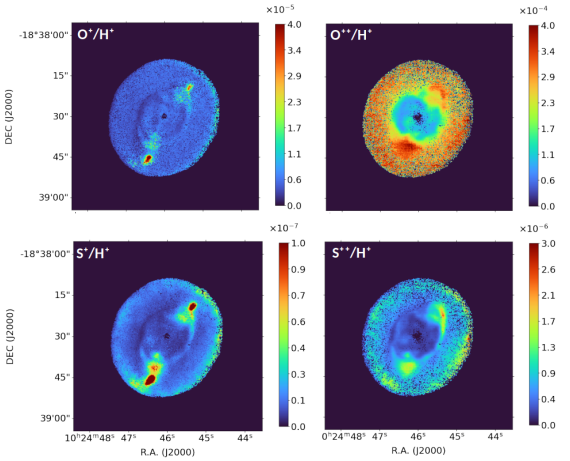

Fig. B.2: Ionic and elemental abundance maps. From left to right and from top to bottom: O^{+}/H^{+}, O^{2+}/H^{+}, S^{+}/H^{+}, and S^{2+}/H^{+}.